ELSEVIER

PII: S0309-1708(97)00003-1

Advances in Water Resources 21 (1998) 401–425

0309-1708/98/$19.00

Coupled groundwater flow and transport: 2. Thermohaline and 3D convection systems

H.-J. G. Diersch[a] **& O. Kolditz**[b]

[a]*WASY Institute for Water Resources Planning and Systems Research Ltd., Waltersdorfer Str. 105, D-12526 Berlin, Germany*
[b]*Institute of Fluid Mechanics and Computer Applications in Civil Engineering, University of Hannover, Appelstr. 9a, D-30167 Hannover, Germany*

(Accepted 31 October 1996)

This work continues the analysis of variable density flow in groundwater systems. It focuses on both thermohaline (double-diffusive) and three-dimensional (3D) buoyancy-driven convection processes. The finite-element method is utilized to tackle these complex non-linear problems in two and three dimensions. The preferred numerical approaches are discussed regarding appropriate basic formulations, balance-consistent discretization techniques for derivative quantities, extension of the Boussinesq approximation, proper constraint conditions, time marching schemes, and computational strategies for solving large systems. Applications are presented for the thermohaline Elder and salt dome problem as well as for the 3D extension of the Elder problem with and without thermohaline effects and a 3D Bénard convection process. The simulations are performed by using the package FEFLOW. Conclusions are drawn with respect to numerical efforts and the appropriateness for practical needs.

Key words: porous media, variable density flow, finite element method, double-diffusive convection, thermohaline convection, three-dimensional Bénard convection.

1 NOMENCLATURE

Latin symbols

	Dimensions	
A	1	L/d aspect ratio
B	1	buoyancy ratio (Turner number)
C, C_0	ML^{-3}	concentration and reference concentration, respectively
C_s	ML^{-3}	maximum concentration
c^f, c^s	$L^2T^{-2}\Theta^{-1}$	specific heat capacity of fluid and solid, respectively
D_d	L^2T^{-1}	medium molecular diffusion coefficient of fluid
D_{ij}	L^2T^{-1}	tensor of hydrodynamic dispersion
d	L	thickness (height)
e	L	extent
e_j	1	components of the gravitational unit vector
f_μ	1	constitutive viscosity relation function
g	LT^{-2}	gravitational acceleration
h	L	hydraulic head
I	1	e/L symmetric intrusion ratio
K	LT^{-1}	isotropic hydraulic conductivity constant
K_{ij}	LT^{-1}	tensor of hydraulic conductivity
k_{ij}	L^2	tensor of permeability
L	L	length
Le	1	Lewis number
N_m	1	basis (shape) function at node m
n_i	1	normal unit vector (positive outward)
p^f	$ML^{-1}T^{-2}$	fluid pressure
Q_C	$ML^{-3}T^{-1}$	sink/source of contaminant mass
Q_C^R	MT^{-1}	lumped balance flux of solute (positive inward)
Q_{EB}	T^{-1}	extended Boussinesq approximation term
Q_T	$ML^{-1}T^{-3}$	sink/source of heat
Q_T^R	ML^2T^{-3}	lumped balance flux of heat (positive inward)

Q_ρ	T^{-1}	sink/source of fluid
q_C^R	$ML^{-2}T^{-1}$	prescribed normal boundary mass flux (positive outward)
q_i^f	LT^{-1}	Darcy flux of fluid
$q_{n_T}^{cond}$	MT^{-3}	normal component of the conductive part of the heat flux (positive outward)
$q_{n_C}^{disp}$	$ML^{-2}T^{-1}$	normal component of the dispersive part of the mass flux (positive outward)
$q_{n_C}^{total}$	$ML^{-2}T^{-1}$	normal component of the convective plus dispersive part of the mass flux (positive outward)
q_{n_h}	LT^{-1}	normal component of the Darcy fluid flux (positive outward)
R, R_d	1	specific retardation factor and its time derivative, respectively
Ra_s, Ra_t	1	solutal and thermal Rayleigh number, respectively
Ra_c	1	critical Rayleigh number
S_o	L^{-1}	specific storage coefficient (compressibility)
T, T_o	Θ	temperature and reference temperature, respectively
V_q^f	LT^{-1}	$\sqrt{q_i^f q_i^f}$ absolute specific Darcy fluid flux
w, w_m		spatial weighting function and weighting function at node m, respectively
x_i	L	Cartesian coordinates, Eulerian spatial coordinate vector

Greek symbols

$\bar{\alpha}$	1	fluid density difference ratio
α_L, α_T	L	longitudinal and transverse thermodispersivity, respectively
$\bar{\beta}$	Θ^{-1}	fluid expansion coefficient
β_L, β_T	L	coefficients of longitudinal and transverse dispersivity of solute, respectively
Γ		boundary
γ	1	error tolerance measure
ΔC	ML^{-3}	concentration difference
ΔT	Θ	temperature difference
Δt_n	T	time step width at time plane n
ϵ	1	porosity
θ	T^{-1}	chemical decay rate
Λ	L^2T^{-1}	thermal diffusivity
λ_{ij}	$MLT^{-3}\Theta^{-1}$	tensor of hydrodynamic thermodispersion
λ_{ij}^{cond}	$MLT^{-3}\Theta^{-1}$	tensor of thermal conductivity
λ_{ij}^{disp}	$MLT^{-3}\Theta^{-1}$	tensor of mechanical thermodispersion
λ^f, λ^s	$MLT^{-3}\Theta^{-1}$	thermal conductivity for fluid and solid, respectively
μ^f, μ_o^f	$ML^{-1}T^{-2}$	dynamic fluid viscosity and reference viscosity, respectively
ρ^f, ρ_o^f	ML^{-3}	fluid density and reference density, respectively
ρ^s	ML^{-3}	solid density
σ	1	$(T - 150)/100$ normalized temperature, T in °C
$\chi(C)$		linear (Henry) or non-linear (Freundlich, Langmuir) sorptivity function
ω	1	C/ρ^f mass fraction
Ω		domain

Subscripts

i, j	spatial Eulerian coordinate (Einstein's summation convention)
l	direction of gravity in the Cartesian coordinate system
m, n, k	nodal points (Einstein's summation convention)
n	time plane or normal direction
o	reference value
p	Gauss point

Superscripts

e	finite element
f	fluid phase
p	predictor value
R	prescribed boundary value
s	solid phase

2 INTRODUCTION

Thermohaline (or double-diffusive) convection processes are connected with the presence of heterogeneous temperature and concentration fields. Thus, convective currents can arise from heat and salinity gradients acting simultaneously (e.g. Refs 2, 8, 52–54, 59, 60, 67, 72, 73). Geophysical applications of thermohaline models can be found for instance in the field of geothermics and waste disposal in salt formations.[24] Thermohaline effects are important for the production of mineralized thermal water, the reinjection of cooled brine into heated deep aquifers connected with geothermal supply technologies, and groundwater movement near salt domes.

Usually, the phenomena of double-diffusive convection (DDC) are related to the presence of both: (1) at least, two properties (substances, thermal energy) stratifying the fluid and having different diffusivities; and (2) opposing effects on the vertical density gradient.[8] Accordingly, different regimes can be distinguished: a 'diffusive regime' occurs if the destabilizing potential comes from the property with the larger diffusivity, e.g. a stable salinity gradient is heated from below. On the other hand, a 'finger regime' exists if the driving (destabilizing) forces are caused by the more slowly diffusing property, e.g. hot saline fluid on top of a stable temperature gradient. Both regimes can also

appear in a differentiated form referred here to as a 'mixed DDC regime' if both properties can destabilize and affect the fluid during the temporal development, e.g. a heavy cool solute sinks down to a region which is heated from below, so a finger regime at the beginning converges more to a diffusive regime over time.

The first part of the paper by Kolditz *et al.*[43] mainly focused on the verification of numerical schemes against available benchmarks for density-coupled convection processes. Established test examples (e.g. the Henry problem, Elder problem, and salt dome problem) are only 2D and single-diffusive (either mass or heat-driven) convection processes. But even for these academic, seemingly simplistic 2D problems a number of discrepancies appear, still, for most recent findings.[55] It has been shown[43] that numerical schemes with their spatial and temporal resolutions can essentially influence computational results. Figure 1 recalls the contradictory results for the Elder problem as well as the salt dome test case obtained by different authors. While Elder[23] and the recomputation done by Voss and Souza[75] used obviously overdiffusive schemes on relatively coarse grids, newer findings[43,55] with refined spatial and temporal discretizations reveal convection patterns that are distinctly different from former work. The flow field now indicates a central upwelling rather than downwelling. More dramatically, Oldenburg and Pruess[55] recently presented new results for the salt dome problem (HYDROCOIN level 1 case 5). They believe they achieved much more accurate solutions for this example. However, their results are fully outside of all results known to date (Fig. 1(b)). In fact, their 'swept forward-type' solutions are suspiciously very near to the pure freshwater case without any density coupling, so TOUGH2's results become widely questionable for problems involving velocity-dependent dispersion effects. A possible reason for this discrepancy is recently indicated by the work of Konikow *et al.*[44] They showed that a salinity pattern of a swept forward type appears if constrained boundary conditions for the salt dome interface are applied (allowing only dispersive release of brine and precluding any convective release of brine). While the study by Konikow *et al.*[44] is more physically motivated it also gives an indication of the importance of a mathematically (numerically) correct handling of boundary conditions for this type of problem, independently of the physical appropriateness or not.

In the past, Galerkin methods, finite differences (FDM) and finite element methods (FEM) have been employed to solve the non-linear coupled balance equations for variable density groundwater problems in 2D. Pinder and Cooper[57] used the method of characteristics. Finite elements based on a primitive *u-v-p*-variable formulation are utilized by Segol *et al.*,[66] Huyakorn and Taylor[38] and Diersch.[13–15] However, the subsequent works desisted from primitive variable approaches because their increased accuracy was shown to be in disproportion to the increased numerical effort and inherent restrictions in formulating boundary conditions. Accordingly, standard formulations succeeded that are based on substituting the Darcy law in the primary balance equations. Recent works devoted to this

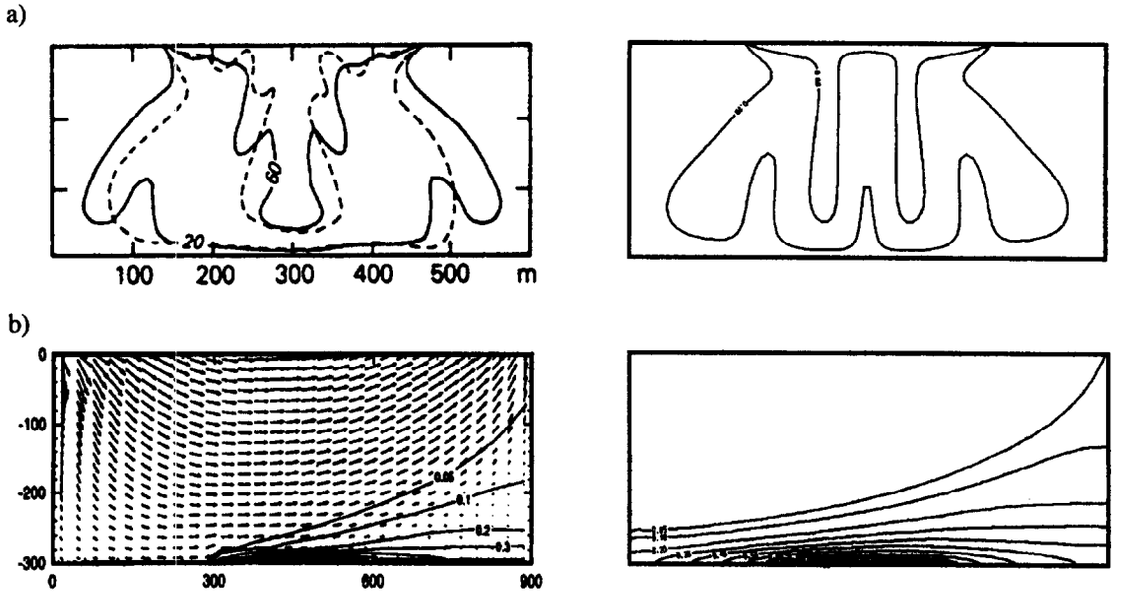

Fig. 1. (a) Simulated concentration pattern at 20 years for the Elder problem with a Rayleigh number of 400; (left) results obtained by the SUTRA simulator (Voss and Souza[75]), (solid curves) and by Elder[23] (dashed curves), and (right) computed by the FEFLOW simulator in agreement with the results attained by ROCKFLOW and TOUGH2 as discussed by Kolditz *et al.*,[43] and (b) salt dome test case: (left) TOUGH2 results[55] against (right) FEFLOW (and ROCKFLOW) findings[43] for steady-state with mechanical dispersion of $\beta_L = 20\,\text{m}$ and $\beta_T = 2\,\text{m}$.

subject are presented, among others, by Frind,[26] Diersch *et al.*,[16] Voss and Souza,[75] Diersch,[17] Hassanizadeh and Leijnse,[31] Herbert *et al.*,[32] Galeati *et al.*,[27], Schincariol *et al.*,[63] Fan and Kahawita,[25] Oldenburg and Pruess,[55] Croucher and O'Sullivan,[12] Zhang and Schwartz,[79] and Kolditz.[42] On the other hand, three-dimensional applications are related to field problems as given by Huyakorn *et al.*,[39] Kakinuma *et al.*[40] and Xue *et al.*[76] and do not consider rigorously the density coupling mechanisms. However, there are prior theoretical and numerical works in three-dimensional free convection problems mostly focused on the (cavity) Horton–Rogers–Lapwood (HRL) problem[54] presented by Holst and Aziz,[34] Zebib and Kassoy,[78] Straus and Schubert,[69,70] Horne,[36] Schubert and Straus,[64] Caltagirone *et al*,[9] Chan and Banerjee,[10] and Beukema and Bruin.[6]

It is obvious from the above that the extension to thermohaline and/or 3D density-coupled convection problems will significantly increase the importance of both getting a physically equivalent process description in the discretized models and overcoming the numerical burden, particularly if aiming at practical problems. In the following, relevant numerical aspects are discussed in the context of the FEM. The developed solution strategies are implemented in the 3D finite-element simulator FEFLOW.[20] FEFLOW is employed to study 2D and 3D, thermohaline and buoyancy-driven convection problems from various perspectives. First, we expand the 2D Elder and salt dome problems to thermohaline processes in order to study thermal influences on groundwater-brine flow systems. Second, we extend the original Elder problem to 3D for both single-diffusive (solutal) and double-diffusive (thermohaline) convection processes to analyze the evolution of 3D pattern formations in comparison with the 2D counterparts. Finally, we consider a Bénard problem as an example of more complex 3D multicellular convection in a porous layer. The presented results for thermohaline and solutal convection systems may provide examples for a comparison analysis in 2D and 3D by using alternative approaches.

3 BASIC EQUATIONS

The governing equations for the coupled mass and heat transport in groundwater (saturated porous medium) are derived from the basic conversion principles for mass, linear momentum, and energy.[43] The following non-linear system finally results[20,22] which has to be solved in two and three dimensions

$$S_o \frac{\partial h}{\partial t} + \frac{\partial q_i^f}{\partial x_i} = Q_\rho + Q_{EB}(C,T) \tag{1}$$

$$q_i^f = -K_{ij} f_\mu \left(\frac{\partial h}{\partial x_j} + \frac{\rho^f - \rho_o^f}{\rho_o^f} e_j \right) \tag{2}$$

$$\left.\begin{aligned} &\frac{\partial}{\partial t}(RC) + \frac{\partial}{\partial x_i}\left(q_i^f C - D_{ij}\frac{\partial C}{\partial x_j}\right) + R\theta C \\ &\quad = Q_C \qquad \text{divergent form} \\ &R_d \frac{\partial C}{\partial t} + q_i^f \frac{\partial C}{\partial x_i} - \frac{\partial}{\partial x_i}\left(D_{ij}\frac{\partial C}{\partial x_j}\right) + (R\theta + Q_\rho)C \\ &\quad = Q_C \qquad \text{convective form} \end{aligned}\right\} \tag{3}$$

$$\left[\epsilon\rho^f c^f + (1-\epsilon)\rho^s c^s\right]\frac{\partial T}{\partial t} + \rho^f c^f q_i^f \frac{\partial T}{\partial x_i} - \frac{\partial}{\partial x_i}\left(\lambda_{ij}\frac{\partial T}{\partial x_j}\right) = Q_T \tag{4}$$

To close the set of balance equations the following constitutive formulations are additionally needed:

$$\left.\begin{aligned} &\rho^f = \rho_o^f\left[1 + \frac{\bar\alpha}{(C_s - C_o)}(C - C_o) - \bar\beta(T - T_o)\right] \\ &h = \frac{p^f}{\rho_o^f g} + x_l \qquad K_{ij} = \frac{k_{ij}\rho_o^f g}{\mu_o^f} \\ &\bar\alpha = \left[\rho^f(C_s) - \rho_o^f\right]/\rho_o^f \qquad f_\mu = \frac{\mu_o^f}{\mu^f(C,T)} \\ &D_{ij} = \left(\epsilon D_d + \beta_T V_q^f\right)\delta_{ij} + (\beta_L - \beta_T)\frac{q_i^f q_i^f}{V_q^f} \\ &R = \epsilon + (1-\epsilon)\chi(C) \quad R_d = \epsilon + (1-\epsilon)\frac{\partial[\chi(C)\cdot C]}{\partial C} \\ &\lambda_{ij} = \lambda_{ij}^{cond} + \lambda_{ij}^{cond} \qquad Q_T = \epsilon\rho^f Q_T^f + (1-\epsilon)\rho^s Q_T^s \\ &\lambda_{ij}^{cond} = \left[\epsilon\lambda^f + (1-\epsilon)\lambda^s\right]\delta_{ij} \\ &\lambda_{ij}^{disp} = \rho^f c^f\left[\alpha_T V_q^f \delta_{ij} + (\alpha_L - \alpha_T)\frac{q_i^f q_i^f}{V_q^f}\right] \end{aligned}\right\} \tag{5}$$

As seen, a hydraulic-head-conductivity-(h-K)-form of the Darcy equation (2), instead of the pressure-permeability-(p-k)-form, is preferred in FEFLOW, which usually permits more convenient formulations of boundary conditions and parameter relations for applications in subsurface hydrology. As a result, the tensor of hydraulic conductivity K_{ij} refers to the reference density ρ_o^f and the reference viscocity μ_o^f, which are, on the other hand, related to the proper reference conditions for the concentration C_o and the temperature T_o. For such a formulation a viscosity relation function f_μ, in eqn (5), appears to include viscosity effects in Darcy's law (2). The following

constitutive polynomial expression is used

$$f_\mu = \frac{\mu_o^f}{\mu^f(C,T)} = \\ = \frac{1 + 1{\cdot}85\omega_{(C=C_o)} - 4{\cdot}1\omega^2_{(C=C_o)} + 44{\cdot}5\omega^3_{(C=C_o)}}{1 + 1{\cdot}85\omega - 4{\cdot}1\omega^2 + 44{\cdot}5\omega^3} \\ \frac{1 + 0{\cdot}7063\sigma - 0{\cdot}04832\sigma^3}{1 + 0{\cdot}7063\sigma_{(T=T_o)} - 0{\cdot}04832\sigma^3_{(T=T_o)}} \qquad (6)$$

which is a combination of empirical relationships given by Lever and Jackson[48] for high-concentration saltwater and by Mercer and Pinder[50] for geothermal processes in the range between 0 and 300°C. In practice, the expansion coefficients $\bar{\alpha}$ and $\bar{\beta}$ of eqn (5) are, in most cases, considered as constant.[54] For the present investigations we shall also use this assumption to maintain an unified parameter basis for comparison purposes. However, it should be mentioned in a geothermal context where large temperature variations occur and buoyancy forces are dominant, that this approach is often not appropriate.[56] Based on the theoretical framework done by Perrochet[56] FEFLOW is also capable of handling a non-linear variable thermal expansion $\bar{\beta}\,(T)$ in the form of a fifth-order polynomial to match the fluid density variation over a wide temperature range with a high accuracy and to satisfy the zero condition (density anomaly) at 4°C. For more details see Diersch.[22]

The divergent form and the convective form of the contaminant mass transport equation (3) (the energy balance equation (4) has already led to a convective form after introducing the temperature) are physically equivalent. Commonly, the convective form of the transport equation is preferred for numerical approximations because simpler boundary-value problems are accessible.

It is known[28,43] the Boussinesq approximation becomes insufficient for large density variations (e.g. at high-concentration brines or high-temperature gradients). The main difference between the Boussinesq approximation and the actual balance quantities is expressed by the additional term $Q_{EB}(C,T)$ in the continuity equation (1) according to

$$Q_{EB}(C,T) = \underbrace{-\epsilon\left(\frac{\bar{\alpha}}{(C_s - C_o)}\frac{\partial C}{\partial t} - \bar{\beta}\frac{\partial T}{\partial t}\right)}_{1} \\ \underbrace{-q_i^f\left(\frac{\bar{\alpha}}{(C_s - C_o)}\frac{\partial C}{\partial x_i} - \bar{\beta}\frac{\partial T}{\partial x_i}\right)}_{2} \qquad (7)$$

which is neglected if the Boussinesq approximation is assumed. The first term in eqn (7) can be omitted if the temporal changes in concentration and/or temperature vanish. However, even the evolving features of a convection process may be thoroughly affected at higher density contrasts (problems of bifurcation, physical instability and hydrodynamic pattern formation). The second term of eqn (7) can be ignored if the density gradient is essentially orthogonal to the velocity vector. This is quite often not a tolerable assumption. Note, eqn (7) has to be modified in the case of a non-linear variable thermal expansion $\bar{\beta}(T)$.[22]

4 SPATIAL DISCRETIZATION

The above eqns (1) to (4) are discretized by the FEM using bilinear or biquadratic elements for 2D, and prismatic pentahedral trilinear or hexahedral trilinear and triquadratic elements for 3D. Finally, it yields the following coupled matrix system

$$\begin{aligned} \boldsymbol{O}\dot{\boldsymbol{h}} + \boldsymbol{S}(\boldsymbol{h},\boldsymbol{C},T)\boldsymbol{h} &= \boldsymbol{F}(\boldsymbol{h},\boldsymbol{q},\boldsymbol{C},\dot{\boldsymbol{C}},T,\dot{T}) \\ \boldsymbol{A}\boldsymbol{q} &= \boldsymbol{B}(\boldsymbol{h},\boldsymbol{C},T) \\ \boldsymbol{P}(\boldsymbol{C})\dot{\boldsymbol{C}} + \boldsymbol{D}(\boldsymbol{q},\boldsymbol{C})\boldsymbol{C} &= \boldsymbol{R}(\boldsymbol{C}) \\ \boldsymbol{U}\dot{T} + \boldsymbol{L}(\boldsymbol{q},T)T &= \boldsymbol{W}(T) \end{aligned} \qquad (8)$$

where $\boldsymbol{h}$, $\boldsymbol{q}$, $\boldsymbol{C}$ and $\boldsymbol{T}$ represent the resulting vectors of the nodal hydraulic head, Darcy fluxes, contaminant concentration and temperature, respectively. The dot means differentiation with respect to time t. The matrices $\boldsymbol{S}$, $\boldsymbol{A}$, $\boldsymbol{O}$, $\boldsymbol{P}$ and $\boldsymbol{U}$ are symmetric and sparse, while $\boldsymbol{D}$ and $\boldsymbol{L}$ are unsymmetric and sparse. The remaining vectors $\boldsymbol{F}$, $\boldsymbol{B}$, $\boldsymbol{R}$ and $\boldsymbol{W}$ encompass the right-hand sides (RHS) of eqns (1) to (4), respectively. The main functional dependence is shown in parenthesis.

The individual finite-element formulations of the matrix system (8) as realized in FEFLOW are summarized in Appendix A. Note, different formulations result for the divergent and the convective forms of the transport equations. Although physically equivalent, they can deliver different numerical solutions due to their different boundary-value formulations.

Another point of view is related to the numerical evaluation of the Darcy fluxes $\boldsymbol{q}$ for a given discretization. The success of a numerical solution for variable density flow problems is essentially dependent on an appropriate choice of suitable schemes for computing derivative quantities from the Darcy equation.

5 CONTINUOUS APPROXIMATION OF VELOCITY FIELDS

The substitution of Darcy fluxes (2) in the continuity eqn (1) gives immediately an equation to determine the unknown hydraulic head $\boldsymbol{h}$ according to the weak

formulation (A3) in Appendix A. If $\boldsymbol{h}$ is known and assuming initial $\boldsymbol{C}$ and $\boldsymbol{T}$ distributions, the fluxes $\boldsymbol{q}$ can be directly computed via Darcy's equation (2). However, a careful handling of derivative quantities is required. As normally done in FEM, piecewise continuous (C^0) basis functions N_m (Appendix A) for the hydraulic head $\boldsymbol{h}$ generate velocity fields $\boldsymbol{q}$ (using derivatives of hydraulic head) that exhibit discontinuities across element boundaries. It results in non-unique values at nodal points. Particularly for buoyancy-influenced flows, discontinuous (non-unique) velocities can cause difficulties (spurious vertical velocities) in the numerical solution due to inappropriate balance approximation of the lower order term $\partial h/\partial x_j$, behaving constantly in an element for the case of linear basis functions, and the higher order gravitational term $[\rho^f(C,T) - \rho_o^f]/\rho_o^f$, varying linearly in an element for linear basis functions, of the RHS of the Darcy eqn (2). This has already been addressed in previous works[29,32,75] and different numerical schemes were proposed to overcome these problems.

Voss and Souza[75] preferred, for the SUTRA code in 2D, a reduced-order approximation of the buoyancy term; actually the concentration is averaged in every element, therefore, the pressure gradient and the concentration distribution have the same spatial variability, practically constant (for linear basis functions). This is called a consistent velocity evaluation. Leijnse[46] showed that such a consistent velocity approximation can be interpreted as an average of the local gravity component in the local directions of a finite element. A generalization of this spatial averaging has recently been presented by Knabner and Frolkovic.[41] Instead of reducing the approximations Herbert *et al.*[32] introduced a mixed interpolation strategy in NAMMU for 2D, where the pressure is approximated by quadratic elements to obtain a linearly distributed pressure gradient which becomes consistent with a linear distribution of the concentration-dependent buoyancy term. Clearly, quadratic basis functions increase the computational expense and, especially for 3D, an alternative approach is preferable.

Taking into consideration that the discretized balance terms of the conservation equations generally provide a different spatial variability (compare the 'diffusion' term against the 'convective' term or a 'reactive' term), a consistent approximation by the FEM means that all terms have to be rigorously weighted at nodal points. As a result, unique values of even discontinuous variables are generated at nodal points. This principle is consequently also applied to the velocity evaluation and leads to approaches referred to as smoothing techniques used in FEFLOW for the present analysis. Lee *et al.*[45] thoroughly discussed both global and local smoothing techniques for derivative quantities. In this light, the weak form of the Darcy equation (A4) in Appendix A can be recognized as a global smoothing procedure which was introduced in the water resources literature by Yel.[77] Today, smoothing techniques have an additional meaning for adaptive methods to compute higher order solutions for an error estimation.[21] Appendix B summarizes the smoothing techniques available in FEFLOW and which are appropriate for the present simulations of coupled phenomena. While global derivative smoothing schemes with a consistent mass matrix require a higher numerical effort, lumped mass smoothing algorithms as well as simpler local smoothing schemes are the most cost-effective approaches and have been shown to be well-suited for the present class of problems. The latter is to be recommended for large 3D problems.

Smoothed velocities of a higher-order approximation lead to a continuous distribution of all velocity components in a mesh. As a consequence, continuous fields also exist along material interfaces, e.g. between media with different hydraulic conductivities, where an interfacial nodal point shares these different media and, naturally, a weighted average of the flux quantities results. Leijnse[46] pointed out that physically unrealistic results can be obtained for cases where the conductivity in adjacent elements differs by more than two orders of magnitude. Indeed, if utilizing such continuous velocity fields from a mesh having an insufficiently adapted interface, discretization particle tracking procedures can lead to poor results if starting pathlines near such an interface location (a particle may effectively be propagated into media with low hydraulic conductivity). On the other hand, a discontinuous velocity field approximation often gives significant problems when a particle crosses an element. Then, a particle can be 'caught' in the interface due to components that have opposite directions across an element edge, as indicated by Sauter and Beusen,[62] who introduced special transition elements with interpolated (smoothed) velocity properties to overcome these difficulties. As the sum, the higher-order approximation of continuous velocities is the most natural approach in the finite element method and needs no ad hoc techniques in adapting interface conditions, provided, however, the interface is appropriately discretized. The necessity for a continuous flow field approximation, also in the context of modelling heterogeneous media, is thoroughly discussed in the work covering mixed hybrid finite element techniques presented by Mosé *et al.*[51] followed by recent discussions given by Cordes and Kinzelbach[11] and Ackerer *et al.*[1]

6 CONSTRAINTS AND RELATED BUDGET ANALYSIS

Constraints of boundary conditions can play an important role in practical modelling of variable density transport. Typically, in saltwater enroachment problems, the boundary conditions of freshwater and

saltwater are dependent on the in/outflowing characteristics essential to a correct mathematical formulation. However, most prior works[27,32,38,44,55,66,75] did not consider such conditions in a rigorous manner. To identify the problem let us consider, for instance, the salt dome flow problem as schematically shown in Fig. 2.

Alternating boundary concentrations appear on the top boundary depending on the dynamic process. As long as water enters the domain it should have a prescribed concentration of freshwater. However, if the water leaves the domain (along the same upper boundary) the concentration on this boundary is unknown and should be computed. Such a description can be easily realized if the entire boundary section is assigned by a freshwater boundary condition of the first kind ($C = C_1^R$) and, at the same time, the boundary will be imposed by a constraint condition in the form of a null minimum mass flux $Q_C^{min_1} \equiv 0$. Such an arrangement guarantees that the freshwater condition remains valid as long as the convective mass flux, being concentration-dependent due to the density variation, points into the domain.

A rigorous handling of such constraints is permitted by a prescription of complementary conditions for each boundary type.[20,22] For instance, the minimum and maximum constraints of a Dirichlet-type concentration will lead to additional conditions in the following form (it reads: the imposed boundary condition $C = C_1^R(t)$ is accepted only if the related mass balance flux Q_C^R (and the related hydraulic head h^R) is within given min-max bounds, if not, these bounds have to be used as new boundary conditions, where the boundary type has to be changed from a first kind into a flux-type boundary condition of a point sink/source Q_C)

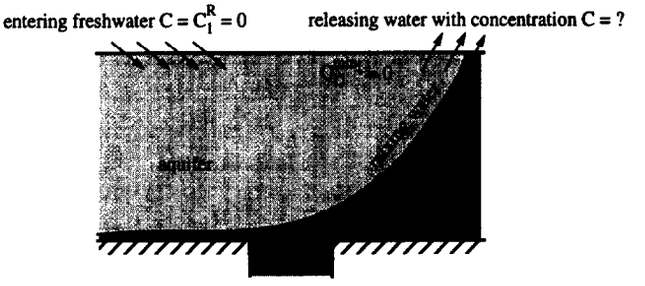

Fig. 2. Application of transport constraints for saltwater intrusion in flowing groundwater over a salt dome.

boundary point (node) instead of the original first kind boundary condition. Similar expression exist for the other types of boundary conditions. This procedure allows the control of concentration at the boundary, depending on both the balanced flow conditions through the boundary (e.g. $Q_C^{min_1} \equiv 0$) and the location of possible free-surface conditions within the bounds h^{min}, h^{max}. The latter is very important for complex mine flooding processes as studied by Diersch *et al.*[19]

The computed fluxes Q_C^R represent lumped (summed-up) mass balance fluxes at nodal points

$$Q_C^R = -\int_\Gamma q_C^R \tag{10}$$

Note, the balance quantities are defined positive inward on Γ. Actually, the specific balance fluxes q_C^R are composed by their convective and dispersive parts according to

$$q_C^R = \underbrace{C^R q_{n_h}^R}_{\text{convective}} - \underbrace{D_{ij}\frac{\partial C}{\partial x_j} n_i}_{\text{dispersive}}$$

$$\text{first kind } C_1^R(t) \text{ only if } \left(\begin{array}{c} Q_C^R < Q_C^{max_1}(t) \\ \text{and} \\ Q_C^R > Q_C^{min_1}(t) \\ \text{and} \\ h^{min_1} \le h^R \le h^{max_1} \end{array} \right)$$

$$\text{else set } Q_C \text{ as an intermediate flux-type condition}$$

$$\text{according to} \quad Q_C = \left(\begin{array}{lllll} Q_C^{max_1}(t) & \text{if} & \{Q_C^R \ge Q_C^{max_1}(t) & \text{and} & h^{min_1} \le h^R \le h^{max_1}\} \\ Q_C^{min_1}(t) & \text{if} & \{Q_C^R \le Q_C^{min_1}(t) & \text{and} & h^{min_1} \le h^R \le h^{max_1}\} \\ 0 & \text{if} & \{h^R < h^{min} & \text{or} & h^R > h^{max}\} \end{array} \right) \tag{9}$$

where Q_C^R is the mass balance flux at the boundary point to be computed while the C_1^R condition is imposed, $Q_C^{max_1}$ and $Q_C^{min_1}$ denote the prescribed time-dependent maximum and minimum bounds, respectively, and Q_C represents a singular mass sink/source to be set at the

In practice, it has been shown to be inappropriate to include the total (convective plus dispersive) flux into the procedure of controlling the constraint conditions because the direction of dispersive fluxes is ambiguous (e.g. the dispersive spreading also occurs against the

flow direction). Accordingly, the balance-based evaluation of fluxes is exclusively related to the convective mass fluxes

$$Q_C^R = -\int_\Gamma q_C^R \approx -\int_\Gamma \left(C^R q_{n_h}^R\right) \tag{12}$$

giving unambiguously directional balance quantities. Similar expressions can be obtained for the balance of convective heat flux, namely

$$Q_T^R \approx -\int_\Gamma \left(\rho^f c^f T^R q_{n_h}^R\right) \tag{13}$$

The computation of the convective part of balance fluxes at each controlling (nodal) point is performed via a budget analysis in a postprocessing step. The basic formulation used for computing the above balance quantities is derived in Appendix C.

7 TEMPORAL DISCRETIZATION AND ITERATIVE SOLUTION PROCESS

In general, for more complex flow processes it cannot be predicted which time steps are allowable with respect to the accuracy requirements. Accordingly, a predefined time step marching strategy is often inappropriate and inefficient. Alternatively, stable fully implicit and semi-implicit two-step techniques, known as the GLS (Gresho–Lee–Sani) predictor-corrector time integrator[7,30] with automatically controlled stepping of

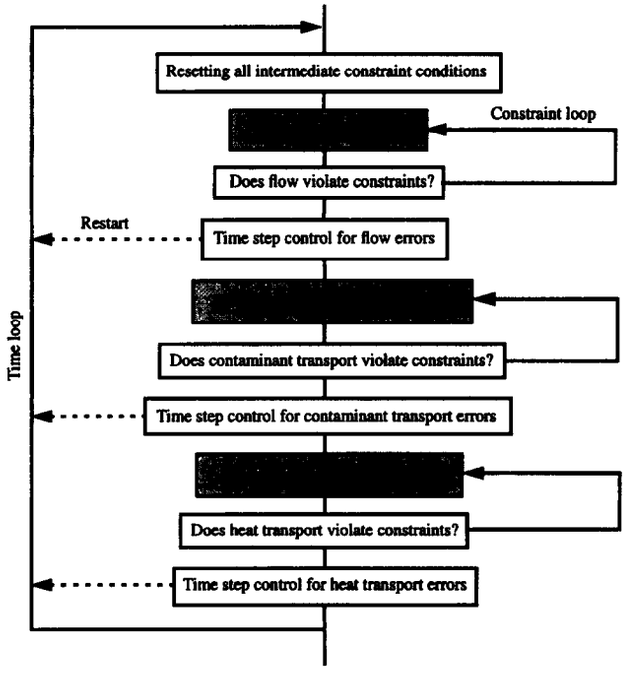

Fig. 3. Adaptive strategy for coupled transient flow, mass and heat transport.

first order by the Forward Euler/Backward Euler (FE/BE) and of second order by the Adams–Bashforth/Trapezoid Rule (AB/TR), have proven to be powerful and accurate strategies, especially for strong nonlinearities and complex situations. At each time step, the convergence tolerance γ directly governs the time-step size. It provides a cost-effective method in that the step size is increased whenever possible and decreased only when necessary due to the error estimates. The GLS scheme is thoroughly described elsewhere.[7,17,18,30] Here, we will only address modified features which are important in the context of the multiple coupling of equations and constraint computation for the present tasks. Note, a full Newton method is embedded into the AB/TR and FE/BE predictor-corrector methods. The overall adaptive solution process is outlined in Fig. 3.

Denoting the time plane by the subscript n and the variable time step width by Δt_n the coupled matrix system (8) is solved in the following 22 raw working steps.

Step 0. Compute the initial acceleration vectors $\dot{\boldsymbol{h}}_n$, $\dot{\boldsymbol{C}}_n$ and $\dot{\boldsymbol{T}}_n$ for $n = 0$ (once per problem)

$$\left.\begin{aligned} \boldsymbol{O}\dot{\boldsymbol{h}}_n &= \boldsymbol{F}(\boldsymbol{h}_n, \boldsymbol{C}_n, \boldsymbol{T}_n) - \boldsymbol{S}(\boldsymbol{h}_n, \boldsymbol{C}_n, \boldsymbol{T}_n)\mathbf{h}_n \\ \boldsymbol{P}(\boldsymbol{C}_n)\dot{\boldsymbol{C}}_n &= \boldsymbol{R}(\boldsymbol{C}_n) - \boldsymbol{D}(\boldsymbol{h}_n, \boldsymbol{C}_n, \boldsymbol{T}_n)\boldsymbol{C}_n \\ \boldsymbol{U}\dot{\boldsymbol{T}}_n &= \boldsymbol{W}(\boldsymbol{T}_n) - \boldsymbol{L}(\boldsymbol{h}_n, \boldsymbol{C}_n, \boldsymbol{T}_n)\boldsymbol{T}_n \end{aligned}\right\} \tag{14}$$

and guess an initial time step Δt_0.

Step 1. Perform explicit predictor solutions by using the AB and FE algorithm, respectively

$$\left.\begin{aligned} \boldsymbol{h}_{n+1}^p &= f_{AB}(\Delta t_n, \Delta t_{n-1}, \dot{\boldsymbol{h}}_n, \dot{\boldsymbol{h}}_{n-1}) \quad \boldsymbol{h}_{n+1}^p = f_{FE}(\Delta t_n, \dot{\boldsymbol{h}}_n) \\ \boldsymbol{C}_{n+1}^p &= f_{AB}(\Delta t_n, \Delta t_{n-1}, \dot{\boldsymbol{C}}_n, \dot{\boldsymbol{C}}_{n-1}) \quad \boldsymbol{C}_{n+1}^p = f_{FE}(\Delta t_n, \dot{\boldsymbol{C}}_n) \\ \boldsymbol{T}_{n+1}^p &= f_{AB}(\Delta t_n, \Delta t_{n-1}, \dot{\boldsymbol{T}}_n, \dot{\boldsymbol{T}}_{n-1}) \quad \boldsymbol{T}_{n+1}^p = f_{FE}(\Delta t_n, \dot{\boldsymbol{T}}_n) \end{aligned}\right\} \tag{15}$$

The detailed description of the functions $f_{AB}()$ and $f_{FE}()$ can be found in Gresho *et al.*,[30] Bixler,[7] and Diersch.[17,18].

Step 2. Do a corrector solution for the flow equation achieved by the TR and BE scheme, respectively

$$\left.\begin{aligned} &\left(\frac{2\boldsymbol{O}}{\Delta t_n} + \boldsymbol{S}(\boldsymbol{h}_{n+1}^p, \boldsymbol{C}_{n+1}^p, \boldsymbol{T}_{n+1}^p)\right)\boldsymbol{h}_{n+1} = \boldsymbol{O}\left(\frac{2}{\Delta t_n}\boldsymbol{h}_n + \dot{\boldsymbol{h}}_n\right) \\ &\qquad + \boldsymbol{F}(\boldsymbol{h}_{n+1}^p, \boldsymbol{C}_{n+1}^p, \boldsymbol{T}_{n+1}^p, \boldsymbol{q}_n, \dot{\boldsymbol{C}}_n, \dot{\boldsymbol{T}}_n) \\ &\left(\frac{\boldsymbol{O}}{\Delta t_n} + \boldsymbol{S}(\boldsymbol{h}_{n+1}^p, \boldsymbol{C}_{n+1}^p, \boldsymbol{T}_{n+1}^p)\right)\boldsymbol{h}_{n+1} = \frac{\boldsymbol{O}}{\Delta t_n}\boldsymbol{h}_n \\ &\qquad + \boldsymbol{F}(\boldsymbol{h}_{n+1}^p, \boldsymbol{C}_{n+1}^p, \boldsymbol{T}_{n+1}^p, \boldsymbol{q}_n, \dot{\boldsymbol{C}}_n, \dot{\boldsymbol{T}}_n) \end{aligned}\right\} \tag{16}$$

Step 3. If constraint conditions are violated, update the matrix system (16) for the new flow boundary values

and restart the flow solution with Step 2. If all constraint limits are satisfied continue with Step 4.

Step 4. Solve the Darcy equation

$$\boldsymbol{A}\boldsymbol{q}_{n+1} = \boldsymbol{B}(\boldsymbol{h}_{n+1}, \boldsymbol{C}^{\mathrm{p}}_{n+1}, \boldsymbol{T}^{\mathrm{p}}_{n+1}) \tag{17}$$

Step 5. Update the new accelerations vectors by 'inverting' the TR and BE, respectively

$$\left.\begin{aligned} \dot{\boldsymbol{h}}_{n+1} &= \frac{2}{\Delta t_n}(\boldsymbol{h}_{n+1} - \boldsymbol{h}_n) - \dot{\boldsymbol{h}}_n \\ \dot{\boldsymbol{h}}_{n+1} &= \frac{1}{\Delta t_n}(\boldsymbol{h}_{n+1} - \boldsymbol{h}_n) \end{aligned}\right\} \tag{18}$$

Step 6. Compute the local truncation error of the approximate flow equation for the AB/TR and FE/BE scheme, respectively

$$\left.\begin{aligned} \boldsymbol{d}^{\mathrm{flow}}_{n+1} &= \frac{\boldsymbol{h}_{n+1} - \boldsymbol{h}^{\mathrm{p}}_{n+1}}{3\left(1 + \dfrac{\Delta t_{n-1}}{\Delta t_n}\right)} \\ \boldsymbol{d}^{\mathrm{flow}}_{n+1} &= \frac{1}{2}(\boldsymbol{h}_{n+1} - \boldsymbol{h}^{\mathrm{p}}_{n+1}) \end{aligned}\right\} \tag{19}$$

Step 7. Predict the potential new time step length from the error estimates of the flow equation

$$\Delta t^{\mathrm{flow}}_{n+1} = \Delta t_n \left(\frac{\gamma}{\|\boldsymbol{d}^{\mathrm{flow}}_{n+1}\|}\right)^{1/\kappa} \tag{20}$$

where κ is 3 for the AB/TR and 2 for the FE/BE scheme, γ is a user-specified error tolerance ($\gamma = 10^{-4} - 10^{-3}$ is typical), and $\|\cdot\|$ is a norm to be chosen as the weighted RMS

$$\|\boldsymbol{d}^{\mathrm{flow}}_{n+1}\| = \left[\frac{1}{NP}\left(\frac{1}{h_{\max}}\sum_i \left(h_{i(n+1)} - h_{i(n)}\right)^2\right)\right]^{1/2} \tag{21}$$

or, alternatively, as the maximum norm

$$\|\boldsymbol{d}^{\mathrm{flow}}_{n+1}\| = \frac{\max_i |h_{i(n+1)} - h_{i(n)}|}{h_{\max}} \tag{22}$$

in which NP is the total number of points and $h_{\max}$ corresponds to the maximum value of the hydraulic head.

Step 8. Tactics for acceptance of the predicted new time step: if the flow solution does not satisfy the prescribed accuracy the time step is reduced by using appropriate formulae.[17,18] and the flow solution is restarted with Step 2. Otherwise, if the accuracy is satisfied, the solution process is continued with Step 9.

Step 9. Perform the corrector solution for the mass transport equation achieved by the TR and BE scheme, respectively

$$\begin{aligned} &\left(\frac{2\boldsymbol{P}(\boldsymbol{C}^{\mathrm{p}}_{n+1})}{\Delta t_n} + \boldsymbol{D}(\boldsymbol{q}_{n+1}, \boldsymbol{C}^{\mathrm{p}}_{n+1}) + \boldsymbol{J}_{\mathrm{p}}(\boldsymbol{C}^{\mathrm{p}}_{n+1})\right)\boldsymbol{C}_{n+1} = \\ &\quad = \boldsymbol{P}(\boldsymbol{C}^{\mathrm{p}}_{n+1})\left(\frac{2}{\Delta t_n}\boldsymbol{C}_n + \dot{\boldsymbol{C}}_n\right) \\ &\qquad + \boldsymbol{J}_{\mathrm{p}}(\boldsymbol{C}^{\mathrm{p}}_{n+1})\boldsymbol{C}^{\mathrm{p}}_{n+1} + \boldsymbol{R}(\boldsymbol{C}^{\mathrm{p}}_{n+1}) \\ &\left(\frac{\boldsymbol{P}(\boldsymbol{C}^{\mathrm{p}}_{n+1})}{\Delta t_n} + \boldsymbol{D}(\boldsymbol{q}_{n+1}, \boldsymbol{C}^{\mathrm{p}}_{n+1}) + \boldsymbol{J}_{p}(\boldsymbol{C}^{\mathrm{p}}_{n+1})\right)\boldsymbol{C}_{n+1} = \\ &\quad = \frac{\boldsymbol{P}(\boldsymbol{C}^{\mathrm{p}}_{n+1})}{\Delta t_n}\boldsymbol{C}_n + \boldsymbol{J}_{p}(\boldsymbol{C}^{\mathrm{p}}_{n+1})\boldsymbol{C}^{\mathrm{p}}_{n+1} + \boldsymbol{R}(\boldsymbol{C}^{\mathrm{p}}_{n+1}) \end{aligned} \tag{23}$$

where $\boldsymbol{J}_{\mathrm{p}}(\boldsymbol{C}^{\mathrm{p}}_{n+1})$ is the partial (tangential) Jacobian matrix based on the predictor which results from the embodied full Newton approach. Its specific expressions depend on the divergent and convective form of the used transport equation, as given by Diersch.[17]

Step 10. If mass constraint conditions are violated, update the matrix system (23) for the new mass boundary values and restart the mass solution with Step 9. Otherwise, continue with Step 11.

Step 11. Update the new acceleration vectors $\dot{\boldsymbol{C}}_{n+1}$ for the concentration similar to Step 5.

Step 12. Equivalently to Step 6 compute the local truncation error of mass transport $\boldsymbol{d}^{\mathrm{mass}}_{n+1}$ based on $(\boldsymbol{C}_{n+1} - \boldsymbol{C}^{\mathrm{p}}_{n+1})$.

Step 13. Estimate the potential new time step from the mass transport computation $\Delta t^{\mathrm{mass}}_{n+1}$, similar to Step 7 by using the error $\boldsymbol{d}^{\mathrm{mass}}_{n+1}$.

Step 14. Accuracy check of mass transport: reject the current mass transport solution and restart at Step 2 with a reduced time width Δt_n if the required accuracy could not be satisfied. Otherwise, continue with the heat transport solution at Step 15.

Step 15. Perform the corrector solution for the heat transport equation accomplished by the TR and BE scheme, respectively

$$\begin{aligned} &\left(\frac{2\boldsymbol{U}}{\Delta t_n} + \boldsymbol{L}(\boldsymbol{q}_{n+1}, \boldsymbol{T}^{\mathrm{p}}_{n+1}) + \boldsymbol{J}_{\mathrm{p}}(\boldsymbol{T}^{\mathrm{p}}_{n+1})\right)\boldsymbol{T}_{n+1} = \\ &\quad = \boldsymbol{U}\left(\frac{2}{\Delta t_n}\boldsymbol{T}_{\mathrm{n}} + \dot{\boldsymbol{T}}_n\right) + \boldsymbol{J}_{\mathrm{p}}(\boldsymbol{T}^{\mathrm{p}}_{n+1})\boldsymbol{T}^{\mathrm{p}}_{n+1} + \mathbf{W}(\boldsymbol{T}^{\mathrm{p}}_{n+1}) \\ &\left(\frac{\boldsymbol{U}}{\Delta t_n} + \boldsymbol{L}(\boldsymbol{q}_{n+1}, \boldsymbol{T}^{\mathrm{p}}_{n+1}) + \boldsymbol{J}_{\mathrm{p}}(\boldsymbol{T}^{\mathrm{p}}_{n+1})\right)\boldsymbol{T}_{n+1} = \\ &\quad = \frac{\boldsymbol{U}}{\Delta t_n}\boldsymbol{T}_n + \boldsymbol{J}_{p}(\boldsymbol{T}^{\mathrm{p}}_{n+1})\boldsymbol{T}^{\mathrm{p}}_{n+1} + \boldsymbol{W}(\boldsymbol{T}^{\mathrm{p}}_{n+1}) \end{aligned} \tag{24}$$

Step 16. If heat constraint conditions are violated update the matrix system (24) for the new heat boundary values and restart the heat transport solution with Step 15. Otherwise, continue with Step 17.

Step 17. Update the new accelerating vectors $\dot{\boldsymbol{T}}_{n+1}$ for the temperature similar to Step 5.

Step 18. Compute the local truncation transport $\boldsymbol{d}_{n+1}^{\text{heat}}$ based on $(\boldsymbol{T}_{n+1} - \boldsymbol{T}_{n+1}^{0})$.

Step 19. Estimate the potential new time step from the heat transport computation $\Delta t_{n+1}^{\text{heat}}$, similar to Step 7 by employing the error $\boldsymbol{d}_{n+1}^{\text{heat}}$.

Step 20. Accuracy check of heat transport: reject the current heat transport solution and restart with Step 2 for a reduced time step if the required accuracy could not be satisfied. Otherwise, continue with Step 21.

Step 21. Determine the new time step length

$$\Delta t_{n+1} = \min\left(\Delta t_{n+1}^{\text{flow}}, \Delta t_{n+1}^{\text{mass}}, \Delta t_{n+1}^{\text{heat}}\right) \tag{25}$$

and restart the time loop with Step 1 as long as the final time is not reached.

As seen above a constraint violation can lead to recycling steps around the matrix solution process for flow, mass and heat transport. The matrix updating gains efficiency if a total reassembly can be avoided. Such a procedure of constraint feedback is generally not restricted in the number of loops. Normally, if constraint conditions are raised two recycles become sufficient.

To solve the resulting large sparse matrix systems (eqs (14), (16), (17), (23), (24)) appropriate iterative solvers for symmetric and unsymmetric equations have to be applied.[3] For the symmetric positive definite flow equations the conjugate gradient (CG) method[33] is successful provided a useful preconditioning is applied. A standard preconditioner, such as the incomplete factorization (IF) technique[49] and, alternatively, a modified incomplete factorization (MIF) technique,[4] based on the Gustafson algorithm, are used. Different alternatives are available for the CG-like solution of the unsymmetric transport equations: a restarted ORTHOMIN[5] (orthogonalization-minimization) method, a restarted GMRES[61] (generalized minimal residual) technique and Lanczos-type methods,[47,71] such as CGS[68] (conjugate gradient square), BiCGSTAB[74] (bi-conjugate gradient stable) and BiCGSTAB[74] (postconditioned bi-conjugate gradient stable). For preconditioning, an incomplete Crout decomposition scheme is currently applied. Commonly, BiCGSTABP is the first choice in our practical simulation of large problems.

8 EXAMPLES OF 2D THERMOHALINE SYSTEMS

8.1 Dimensionless parameters

From a dimensional analysis of the governing balance equations one can derive the following dimensionless parameters[54] to characterize the convection processes.

Solutal Rayleigh number Ra_s

$$Ra_{\text{s}} = \frac{\frac{\bar{\alpha}}{(C_{\text{s}} - C_{\text{o}})}\Delta C K d}{\epsilon D_{\text{d}}} \tag{26}$$

Thermal Rayleigh number Ra_t

$$Ra_{\text{t}} = \frac{\bar{\beta}\Delta T K d}{\Lambda} \qquad \Lambda = \frac{\epsilon\lambda^{\text{f}} + (1-\epsilon)\lambda^{\text{s}}}{\rho^{\text{f}} c^{\text{f}}} \tag{27}$$

Lewis number Le

$$Le = \frac{\Lambda}{\epsilon D_{\text{d}}} \tag{28}$$

Buoyancy ratio (Turner number) B

$$B = \frac{\frac{\bar{\alpha}}{(C_{\text{s}} - C_{\text{o}})}\Delta C}{\bar{\beta}\Delta T} \tag{29}$$

Accordingly, the relation between the solutal and thermal Rayleigh number is given by

$$Ra_{\text{s}} = BLeRa_{\text{t}} \tag{30}$$

From perturbation analysis along the thermohaline Horton–Rogers–Lapwood (HRL) problem[54] the critical Rayleigh number Ra_c is composed of solutal and thermal influences. It can be shown for the HRL problem that the boundary between stable and unstable convection possesses a straight line, namely

$$Ra_{\text{c}} = Ra_{\text{s}} + Ra_{\text{t}} \tag{31}$$

The critical Rayleigh number Ra_c depends on boundary conditions, geometry and anisotropy. A first critical number Ra_{c1} describes the onset of convection in the form of stable stationary rolls, which is normally given by $4\pi^2$. A further increase of the Rayleigh number leads to a second critical stage characterized by Ra_{c2}. For this regime no more stationary conditions exist and fluctuating (oscillatory) transient convective patterns appear. Ra_{c2} is only known from numerical studies,[35,37,58,65] where a value of about 390 is reported. For 3D cases it has been found that the final convective structures are dependent on the initial conditions. Stable convection could be recognized only if raised as 2D roll cells. Otherwise, the 3D state has been found to be unstable from the beginning,[78] soon above criticality.

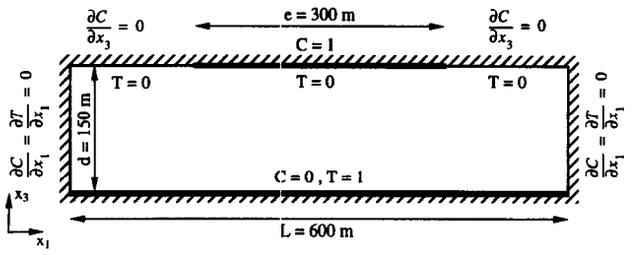

Fig. 4. Definition of the 2D thermohaline Elder problem (modified from Voss and Souza[75]).

8.2 The 2D thermohaline Elder problem

8.2.1 Definition of the problem

The 2D saline Elder problem[43] is expanded to a thermohaline convection process if the salinity field is augmented by a thermal distribution as defined in Fig. 4. The geometry is given by the aspect ratio $A = L/d$ of 4 and a so-called intrusion ratio $I = e/L$ of 0·5. While the homogeneous aquifer is permanently heated from below, the salinity gradient acts from above. The normalized concentration on the top of aquifer is greater than zero in the central section. On the bottom of the aquifer the salinity is held at zero. On the other hand, the top and bottom boundaries are held at constant temperatures as indicated in Fig. 4. Otherwise, all remaining boundary portions are considered impervious for solute and adiabatic (insulated) for heat. All boundaries are impervious for fluid flow. As a reference for the hydraulic head a single boundary value of $h = 0$ has to be set at one mode (normally in the centre of the mesh). The used model parameters are summarized in Table 1.

As stated above, such a formulation of the thermohaline Elder problem can be considered as a mixed DDC regime where a finger regime dominates at the beginning (cool salinity sinks down) and later a more diffusive regime occurs (downsunk salinity is heated from below). The finite element meshes as shown in Fig. 5, which have proven to be capable of attaining convergent solutions for the Elder problem,[43] are also used for the following investigations.

8.2.2 Results and discussion

The basis for comparison is the thermohaline simulation for the pure saline free convection, *i.e.* $Ra_t = 0$ and $B = \infty$, as presented in the first part of this paper.[43] It meets the best numerical approximation available for this case: divergent formulation of the mass transport equation, extended Boussinesq approximation, Galerkin-FEM, and a predictor-corrector AB/TR time integrator. As the convergence tolerance γ a value of 10^{-3} is used both for head h, salinity C and temperature T based on a RMS error norm (cf. eqn (21)).

To study the growing influence of thermohaline convection more in detail we consider the computational results using mesh A for decreasing buoyancy ratios $B = \infty$, 5, 4, 3, 2 as exhibited in a series in Fig. 6. While the results for $B = 5$ (Fig. 6(b)) are still rather similar

Table 1. Simulation parameters for the 2D thermohaline Elder problem

Symbol	Quantity	Value	Unit
A	aspect ratio	4	1
B	buoyancy ratio (Turner number)	1, 2, 3, 4, 5	1
C_0	reference concentration	0	g l^{-1}
$c^f\rho^f$	thermal capacity of fluid	$4{\cdot}2 \times 10^6$	J m^{-3} K^{-1}
D_d	molecular diffusion coefficient	$3{\cdot}565 \times 10^{-6}$	m^2 s^{-1}
d	thickness (height)	150	m
e	extent of intrusion	300	m
f_μ	viscosity relation function	1	1
I	symmetric intrusion ratio	0·5	1
K	hydraulic conductivity	$4{\cdot}753 \times 10^{-6}$	m s^{-1}
L	length	600	m
Le	Lewis number	1	1
Ra_s	solutal Rayleigh number	400	1
Ra_t	thermal Rayleigh number	400, 200, 133.3, 100, 80	1
T_0	reference temperature	0	K
ΔT	temperature difference	400, 200, 133.3, 100, 80	K
α_L	longitudinal thermodispersivity	0	m
α_T	transverse thermodispersivity	0	m
$\bar{\alpha}/C_s$	density ratio	0·2	1
β_L	longitudinal dispersivity of solute	0	m
β_T	transverse dispersivity of solute	0	m
$\bar{\beta}$	thermal expansion coefficient	5×10^{-4}	K^{-1}
ϵ	porosity	0·1	1
Λ	thermal diffusivity	$3{\cdot}565 \times 10^{-7}$	m^2 s^{-1}
λ^f	thermal conductivity of fluid	0·65	J m^{-1} s^{-1} K^{-1}
λ^s	thermal conductivity of solid	1·591	J m^{-1} s^{-1} K^{-1}

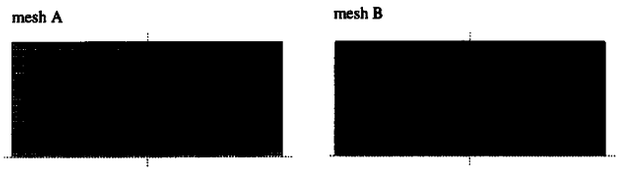

Fig. 5. Finite element meshes used: mesh A consisting of 4400 element and 4539 nodes, refined mesh B with 9900 elements and 10 108 nodes.

to the pure (asymptotic) saline convection at $B = \infty$ (Fig. 6(a)), beginning with $B = 4$, the influence of the superimposing thermal convection on the salinity distribution becomes apparent (Figs 6(c)–(e)). There are no more monotonic changes in the salinity pattern. Surprisingly, salinity distributions reveal asymmetric characteristics at longer times when the influence of thermal convection becomes stronger as seen at $B = 2$ in Fig. 6(e).

To check the influence of spatial resolution the computations are repeated with the refined mesh B. The long-term salinity pattern for small buoyancy ratios is illustrated in Fig. 7. Now, symmetric salinity distributions appear for $B = 4$ (Fig. 7(a)) and $B = 2$ (Fig. 7b)). A comparison with the coarser mesh counterparts of Fig. 6 reveals further qualitative changes in the pattern evolution. The case with an equilibrium of solutal and thermal buoyancy effects for $B = 1$ (Fig. 7(c)) gives again asymmetric distributions of salinity. Note, the effective Rayleigh number is here already 800 ($Ra = Ra_s + Ra_t$) where transient disturbances should take influence. However, there is apparently no physical reason for a broken symmetry and mesh effects are likely responsible for such an asymmetric evolution. It is obvious, at sufficiently high Rayleigh numbers that each initially small disturbance which is not perfectly symmetric can evoke asymmetry, which grows over a longer period. Moreover, in the numerical solution process such disturbances can be caused for example, by inappropriate spatial discretizations, the remaining errors in solving the matrix system by iterative techniques or by round-off errors arising in computing the physically unstable process. On the other hand, in a physical experiment or in real sites the trigger of asymmetry may be an initially disturbed distribution or due to non-homogeneous materials.

It seems that the numerical solutions reflect the physical instabilities which are most apparent for the thermohaline system if the solutal and thermal effects are nearly equilibrated ($B = 1$). It becomes obvious that modelling of such unstable thermohaline systems will be very expensive, especially in 3D.

Finally, Fig. 8 presents both the stimulated temperature and salinity distributions for the case of $B = 4$. It demonstrates how the salinity evolution in a thermohaline convection process is related to specific pattern formations of the temperature field.

8.3 The 2D thermohaline salt dome problem

8.3.1 Definition of the problem

The considered test case is an idealization of the flow over a salt dome,[32,43,44,55] where the geometry is greatly simplified. The geometry and boundary conditions used are shown in Fig. 9. The cross-section of the model extends horizontally 900 m and vertically 300 m having an aspect ratio A of 3. The aquifer is considered to be homogeneous and isotropic. The hydraulic head varies linearly on the top of the aquifer. All remaining boundaries are impervious to flow. The salinity on the top is taken equal to zero (freshwater) over the entire boundary. Additionally, a minimum mass flux constraint condition of $Q_C^{\min_1} \equiv 0$ is imposed. This ensures that the freshwater condition is only valid if the flow enters the domain. The middle section of the aquifer base represents the cap of the salt dome having a relative salt concentration equal to unity. The thermohaline extension of the salt dome problem concerns a superimposition of a thermal gradient acting upward and it tends to destabilize the brine pool due to the arising buoyant forces. Accordingly, the bottom of the aquifer is assigned by a constant normalized temperature of $T = 1$, while the top boundary is imposed by a normalized temperature of zero ($T = 0$). Again, the upper boundary is additionally constrained by a minimum heat flux of zero $Q_T^{\min_1} \equiv 0$ which permits a control of the boundary conditions for inflowing and outflowing situations. The side walls of the domain are regarded as impervious for solute mass and adiabatic (insulated) for heat. The model parameters are summarized in Table 2. According to the DDC classification as stated above, the formulation of the thermohaline salt dome problem is one of a diffusive regime where the buoyancy force is caused by heat, which has a larger diffusivity than salt.

The finite element mesh as shown in Fig. 10 is used for the simulations of the thermohaline salt dome problem. The predictor–corrector AB/TR time integrator with a RMS-based convergence tolerance γ of 10^{-3} is applied.

8.3.2 Results and discussion

Simulated results of the salt dome problem at a time of 100 years for different buoyancy ratios B are shown in Fig. 11. It reveals that the temperature effect on the saltwater distribution remains negligible or small if compared with the single-diffusive results[43] at higher buoyancy ratios B. As seen for $B = 2$, however, if the buoyancy ratio becomes smaller, vigorous temperature influences on the brine pattern result in form of a 'wavy' salinity field caused by the thermal buoyancy.

To illustrate how such a thermal effect on the brine flow is evolved a series of salinity and temperature patterns are outlined in Fig. 12 for the case of $B = 2$. The 'wavy' salinity characteristics are triggered in front of the salt wedge by thermally driven eddies. As

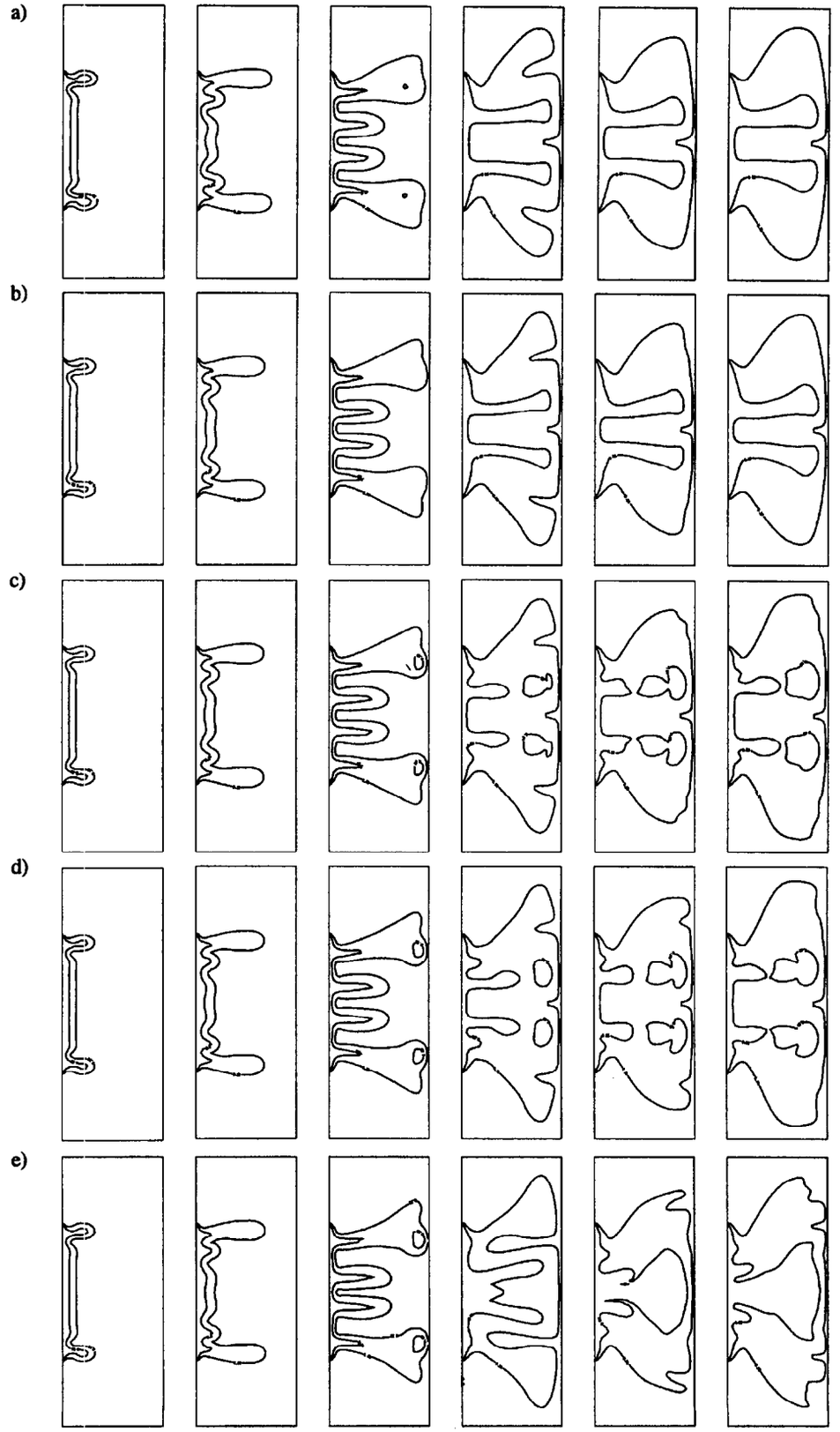

Fig. 6. Influence of thermohaline convection: computed salinity distributions of 0·2 and 0·6 normalized isochlors at 1, 2, 4, 10, 15 and 20 years (from left to right) for different buoyancy ratios (a) $B = \infty$; (b) $B = 5$; (c) $B = 4$; (d) $B = 3$; and (e) $B = 2$ by using mesh A.

expected, it leads to an increased saltwater effluent on top of the aquifer. Note, that a buoyancy ratio of 2 implies an already large temperature difference for a high-concentration brine and, accordingly, corresponds to an extreme situation. It should be mentioned that for the real site behind the present salt dome problem such high temperatures corresponding to $B = 2$ may be unlikely to occur in practice. However, the variants can be valuable as test cases to study the effects of high temperatures, which may, for instance, arise in the vicinity of a disposal facility for heat-emitting waste.

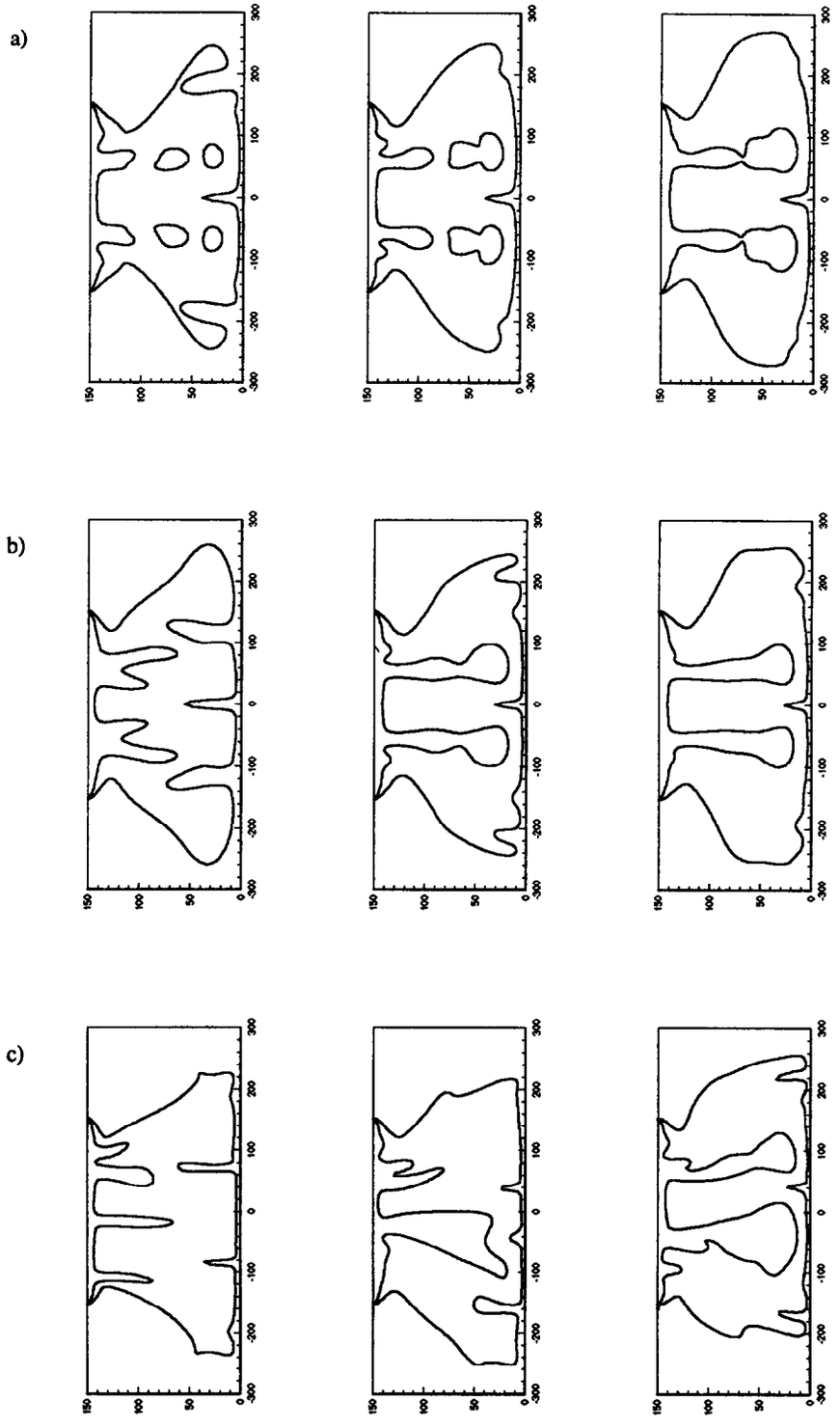

Fig. 7. Mesh effects: computed salinity distributions of 0·2 and 0·6 normalized isochlors at 10, 15 and 20 years (from left to right) for different buoyancy ratios (a) $B = 4$; (b) $B = 2$; and (c) $B = 1$ by using mesh B.

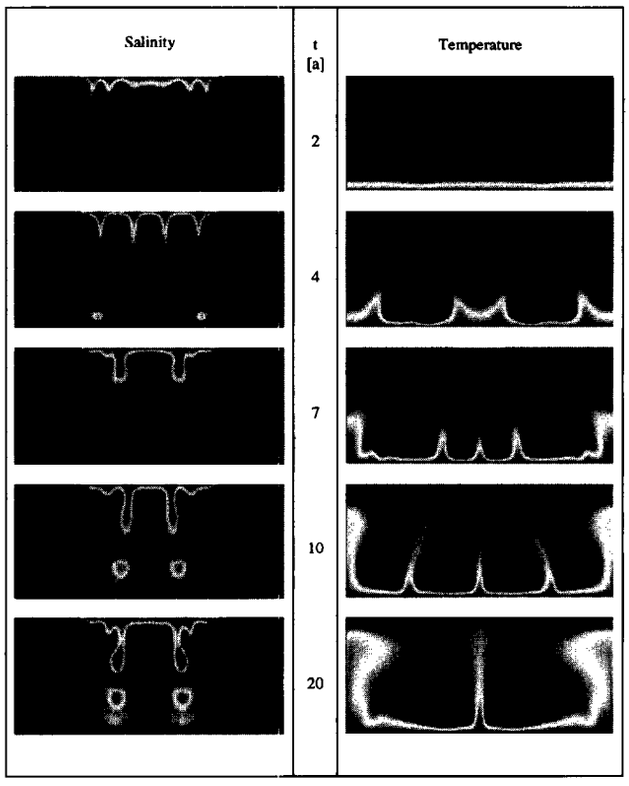

Fig. 8. Computed distributions of salinity and temperature at several times for $B = 4$ using mesh A.

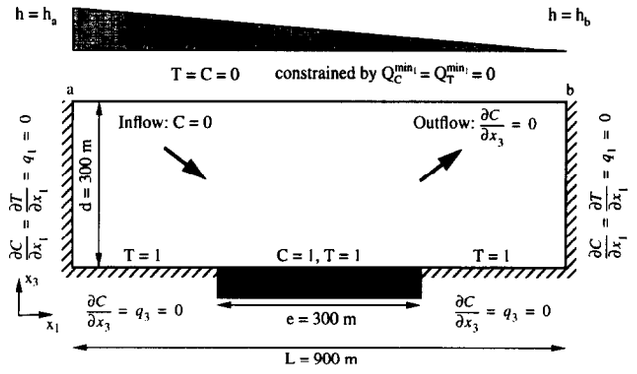

Fig. 9. Definition of the 2D thermohaline salt dome problem (modified from Herbert *et al.*[32]).

9 EXAMPLES OF 3D CELLULAR CONVECTION

9.1 The 3D Elder problem for single-diffusive (solutal) and double-diffusive (thermohaline) convection

9.1.1 Definition of the problem

Originally, the Elder problem[23] refers to a 2D cross-sectional convection process in a fluid-saturated porous layer. As a result, only 2D roll cells can appear. Now, interest is focused on adequate 3D situations. For this purpose the Elder problem is expanded for both single-diffusive and double-diffusive applications in a porous box consisting of a square base ($L \times L$) and height d. This box has the same cross-sections along the Cartesian

Table 2. Simulation parameters for the 2D thermohaline salt dome problem

Symbol	Quantity	Value	Unit
A	aspect ratio	3	1
B	buoyancy ratio (Turner number)	2, 3, 5	1
C_0	reference concentration	0	g l^{-1}
$c^f\rho^f$	thermal capacity of fluid	$4{\cdot}2 \times 10^6$	J m^{-3} K^{-1}
$c^s\rho^s$	thermal capacity of solid	$2{\cdot}52 \times 10^6$	J m^{-3} K^{-1}
D_d	molecular diffusion coefficient	$1{\cdot}39 \times 10^{-8}$	m^2 s^{-1}
d	thickness (height)	300	m
e	extent of intrusion	300	m
f_μ	viscosity relation function	1	1
h_a	hydraulic head at point a	10·228	m
h_b	hydraulic head at point b	0	m
K	hydraulic conductivity	$1{\cdot}0985252 \times 10^{-5}$	m s^{-1}
Le	Lewis number	217	1
Ra_s	solutal Rayleigh number	$2{\cdot}4 \times 10^5$	1
Ra_t	thermal Rayleigh number	547, 365, 219	1
T_0	reference temperature	1	K
α_L	longitudinal thermodispersivity	20	m
α_T	transverse thermodispersity	2	m
$\bar{\alpha}/C_s$	density ratio	0·2036108	1
β_L	longitudinal dispersivity of solute	20	m
β_T	transverse dispersivity of solute	2	m
$\bar{\beta}$	thermal expansion coefficient	5×10^{-4}	K^{-1}
ϵ	porosity	0·2	1
Λ	thermal diffusivity	$6{\cdot}024 \times 10^{-7}$	m^2 s^{-1}
λ^f	thermal conductivity of fluid	0·65	J m^{-1} s^{-1} K^{-1}
λ^s	thermal conductivity of solid	3	J m^{-1} s^{-1} K^{-1}

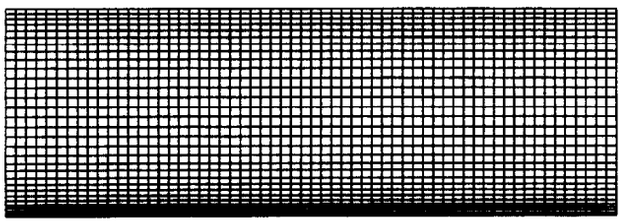

Fig. 10. Finite element mesh used for 2D thermohaline salt dome problem consisting of 1920 elements and 2013 nodes.

axes as defined in Fig. 4 for the 2D sketch. Boundary conditions and measures are identical to the 2D case shown in Fig. 4. Now, salinity is held constant, in an areal extent, on the top and bottom of the porous box. The used parameters correspond to those given in Table 1.

The box is discretized by hexahedral trilinear finite elements as displayed in Fig. 13. To reduce the computation effort only a quarter of the discretized domain is actually simulated. It is based on the assumption that symmetric planes occur for the studied range of Rayleigh numbers. Both AB/TR and FE/BE time marching with a RMS-based convergence tolerance γ of 10^{-3} have been tested. For the long-term simulations and the chosen spatial resolution the second-order AB/TR scheme with a full Newton method becomes sensitive and produces oscillations at later simulation times. On the other hand, the first-order FE/BE scheme with full Newton method has proven to be more stable and robust and, therefore, it is preferred for the present 3D simulations. Generally, Galerkin-FEM (i.e. no upwinding) is used. To simulate the convection process over a period of 100 years the FE/BE scheme takes 641 time steps for the single-diffusive problem and 965 time steps for the double-diffusive (thermohaline) problem (excluding restarted steps).

9.2.2 Results and discussion

The 3D free convection process is similar to the 2D counterpart, with some interesting new features. To give more insight into the physics of the 3D convection process, Fig. 14 shows the evolution of salinity from different views. The 3D cut-away images (left column of Fig. 14) display the progressing fingering characteristics in the 3D space. Similar to the 2D case we also find an upwelling salinity pattern in the centre of the box at the given time stages. The 3D influence also becomes apparent in the two horizontal views at an upper elevation of $0{\cdot}9\,d$ (135 m) and the middle horizon of $0{\cdot}5\,d$ (75 m) as shown in Fig. 14. At the beginning, the quadratic geometry of the intrusion area on top is visible in the convection pattern. Fingers appear around the border of the intrusion area and 'blobs' grow down at the four corners. The quadratic pattern evolves into more complicated multicellular formations via a number of characteristic stages. More 'blobs' appear up to the time when the salinity reaches the bottom. Then, the structures begin to fuse and the pattern is completely reformed. After this phase a convection pattern remains which has a characteristic diagonal 'star' form. This 'star' is a result of the geometry of the square intrusion area. It becomes clear that the final formations have a strong dependency on the geometric relations.

An illustration of the pattern evolution in 3D space is given in Fig. 15 where isosurfaces of the 50% salinity are shown at characteristic time stages. Up to a time of about 4 years the salinity primarily sinks down and forms a dissected finger formation. At later

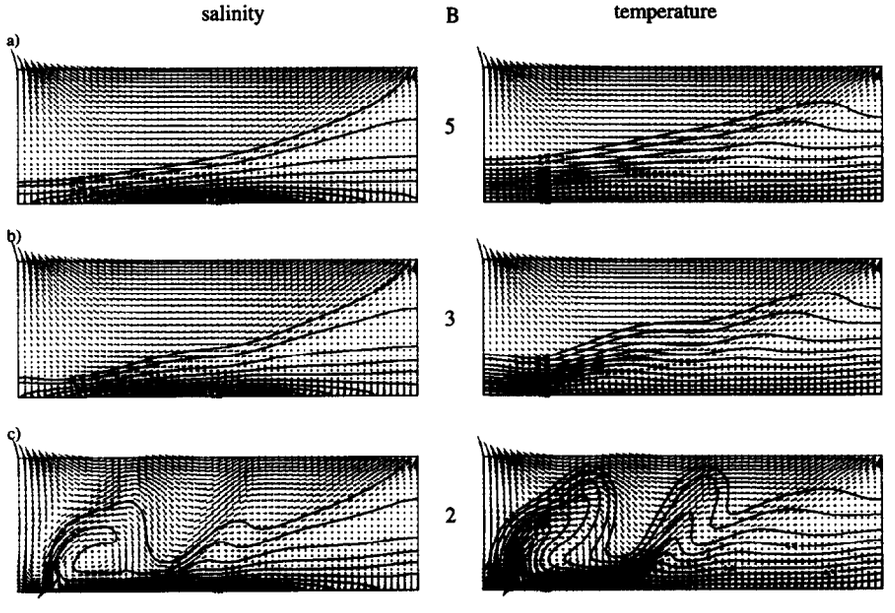

Fig. 11. Evolution of the thermohaline convection system: computed salinity and temperature distributions at 100 years for different buoyancy ratios (a) $B = 5$; (b) $B = 3$; and (c) $B = 2$.

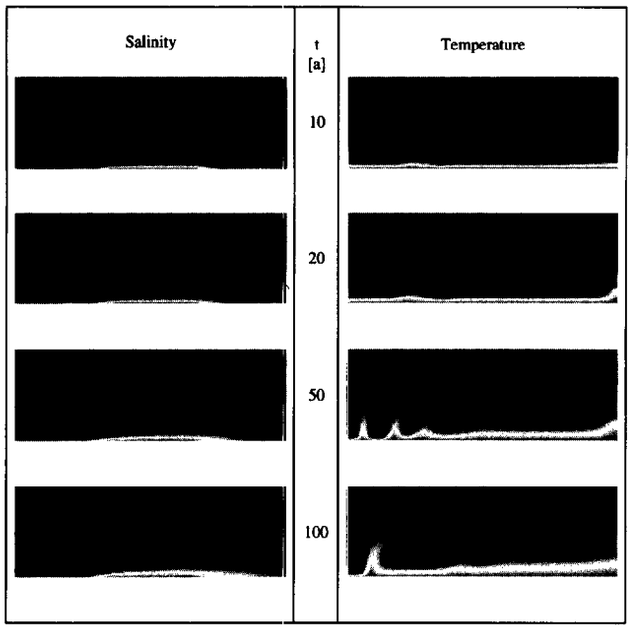

Fig. 12. Evolution of the thermohaline convection system: computed salinity and temperature distributions at several times for a buoyancy ratio of $B = 2$.

time the upper part contracts and forms the typical diagonal 'star', while larger 'blobs' are getting fused below.

The 3D thermohaline Elder problem has been simulated for a buoyancy ratio of $B = 5$, where the solutal Rayleigh number Ra_s is again 400. The 3D distributions of the computed salinities and temperatures for up to 20 years are displayed in Fig. 16. In contrast to the single-diffusive formation (cf. Fig. 14) the salinity pattern appears more diffusive at later times when the temperature field affects the convection system. Then, the thermally buoyant forces accelerate the contraction process of the sinking salinity plume in the centre. In the final stage, while the single-diffusive convection still provides an upwelling flow in the centre, the thermohaline convection process reveals a single downwelling characteristics for the

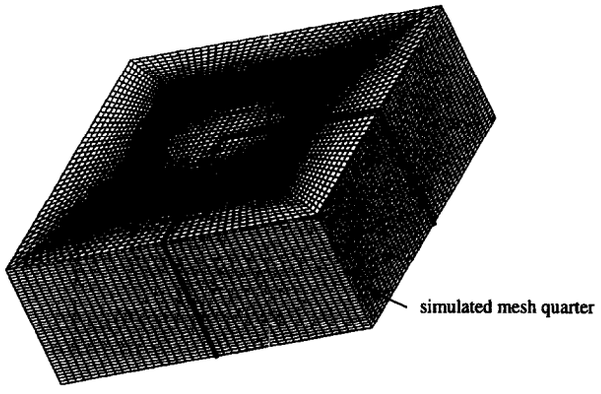

Fig. 13. Total finite element mesh for the 3D Elder problem: only a quarter of the mesh is actually used in the computation. This quarter consists of 48 000 hexahedral elements and 51 701 nodes.

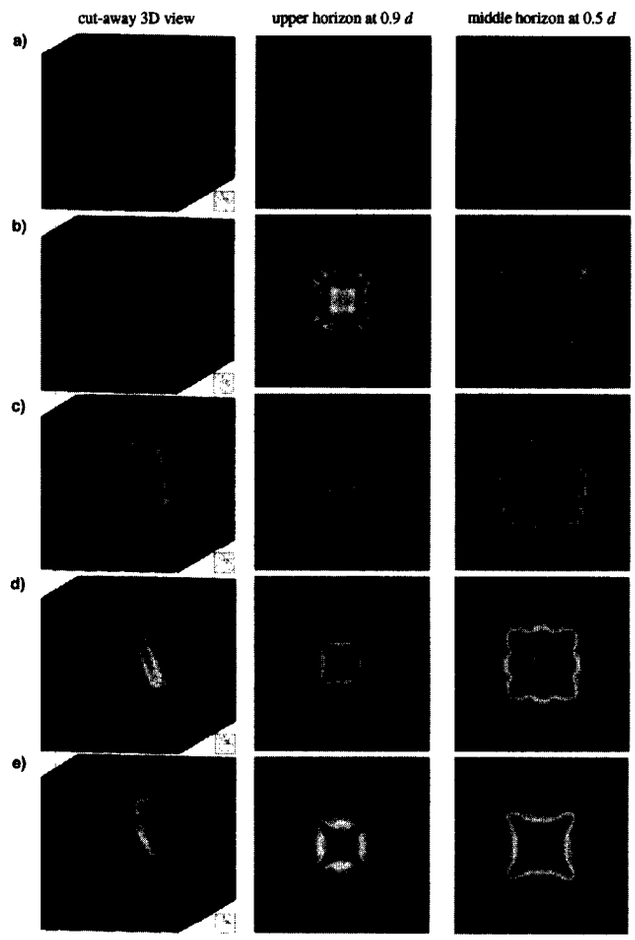

Fig. 14. Computed salinity patterns of the 3D Elder problem at times of (a) 1; (b) 2; (c) 4; (d) 10 and (2) 20 years.

salinity (see Figs 15 and 17). As seen, the most heated water is buoyantly affected outside and around the denser salinity core, where the isotherms come to the upper locations. These mutual influences between salinity and temperature are more apparent in Figs 17 and 18 for the computed isosurfaces of salinity and temperature, respectively.

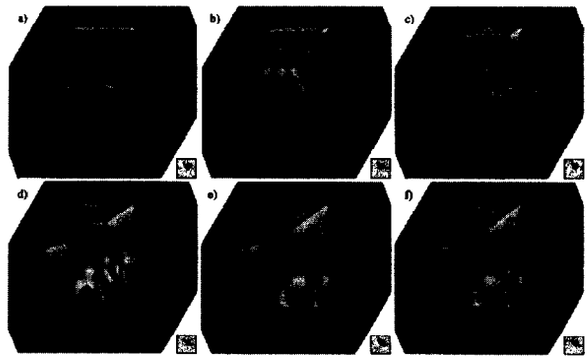

Fig. 15. Computed 3D isosurfaces of 50% salinity for the 3D Elder problem (viewing into the box from bottom to top) at times of (a) 1; (b) 2; (c) 4; (d) 10; (e) 15 and (f) 20 years.

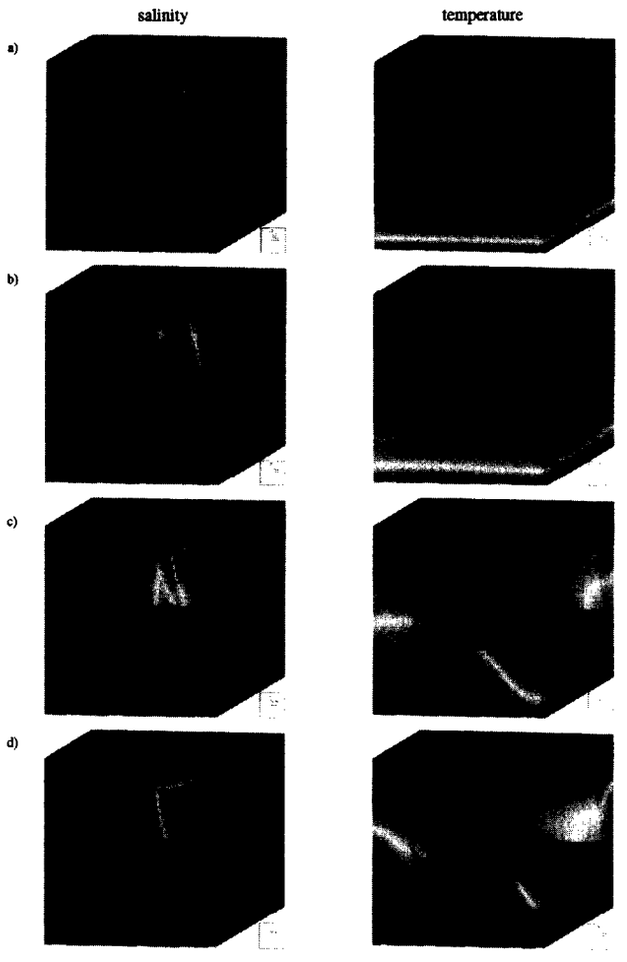

Fig. 16. Cut-away views of simulated salinity (left) and temperature (right) distributions for the 3D thermohaline Elder problem at buoyancy ratio of $B = 5$ and times of (a) 2; (b) 4; (c) 10 and (d) 20 years.

9.2 The 3D Bénard convection

9.2.1 Definition of the problem

Three-dimensional convective pattern formations in domains representing a thin porous layer, i.e. for large aspect ratios A, can be considered as a porous medium equivalent of Bénard convection. As Elder[23] studied such a problem in 2D — referred to as the 'long-heater problem' – for a Rayleigh number of 200, an aspect ratio A of 10, and an intrusion ratio I of 0·8. We extend this 'long-heater problem' to 3D similar to the above Elder problem. The remaining simulation parameters correspond to that of the original Elder problem described in the first part of this paper.[43] Due to the multicellular convection process in the porous layer, a more refined spatial discretization is needed compared with the 3D Elder problem above. Moreover, no assumptions of symmetry are made and, accordingly, the domain has to be fully discretized. The finite element mesh for the problem consists of 220 000 ($100 \times 100 \times 22$) hexahedral trilinear elements containing 234 623 ($101 \times 101 \times 23$) nodes. Again, for the temporal discretization the FE/BE predictor-corrector scheme with the full Newton method and a RMS-based convergence tolerance γ of 10^{-3} is applied to the simulation.

9.2.2 Results and discussion

The striking features of 3D Bénard convection development are shown in Fig. 19. The initial motion is characterized by a rectangular string of end-cells where, at the four corner points, the most intensive growths of 'blobs' can be observed. It is followed by a growth of cells starting from the ends of the intrusion area on top. At these times a remarkable feature of the 3D convection process is the annular roll pattern formation. At smaller times the cell structures are rather complex (Fig. 19(b)) showing the birth of subcellular eddies both across and along the annular structure. Due to the smaller Rayleigh number the nonroll-like perturbations are smoothed at larger times and the convection process results in a highly regular pattern of ring structures.

10 Closure

The finite-element method is applied to simulate variable density flow processes in 2D and 3D groundwater systems. The described solution strategies as implemented in the simulator FEFLOW are more general and are primarily developed to tackle complex practical applications where solutal and/or thermal density effects play an important role. However, before more complex field situations can be studied the chosen methods and codings have to be extensively tested over a wider spectrum of this important class of non-linear problems. In this context the aim of the present paper is mainly proving and benchmarking of the simulations along examples where comparable results are available, or if not, the obtained results are to be supposed as a comparison basis for further studies. We have chosen the Elder and salt dome problem (HYDROCOIN case 5 level 1) as well suited and representative examples. They allow us both to participate in the process of resolving partly contradictory results given in the literature and to expand (or generalize) the 2D solutions to three dimensions and additional coupling phenomena from a well-documented and accepted source. The extensions concern thermohaline and multicellular convection processes in 2D and 3D. Unfortunately, to date both numerical and experimental results of 3D and thermohaline convection are rare and we are mostly dependent on an incremental procedure in comparing and interpreting the results among one another. In this context we found similarities and also interesting new features regarding the pattern formations of the buoyancy-driven convection processes.

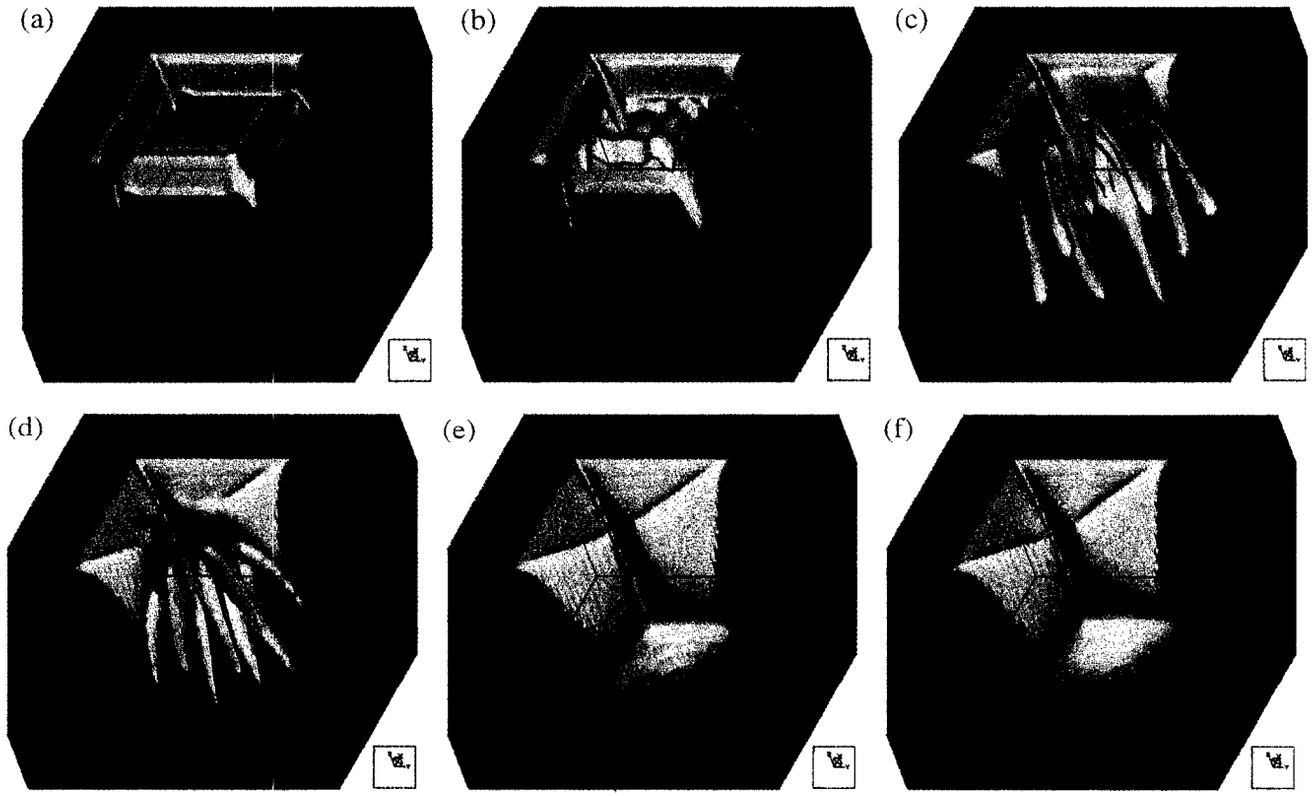

Fig. 17. Computed 3D isosurfaces of 50% salinity for the 3D thermohaline Elder problem (viewing from bottom to top) at $B = 5$ and times of (a) 1; (b) 2; (c) 4; (d) 10; (e) 15 and (f) 20 years.

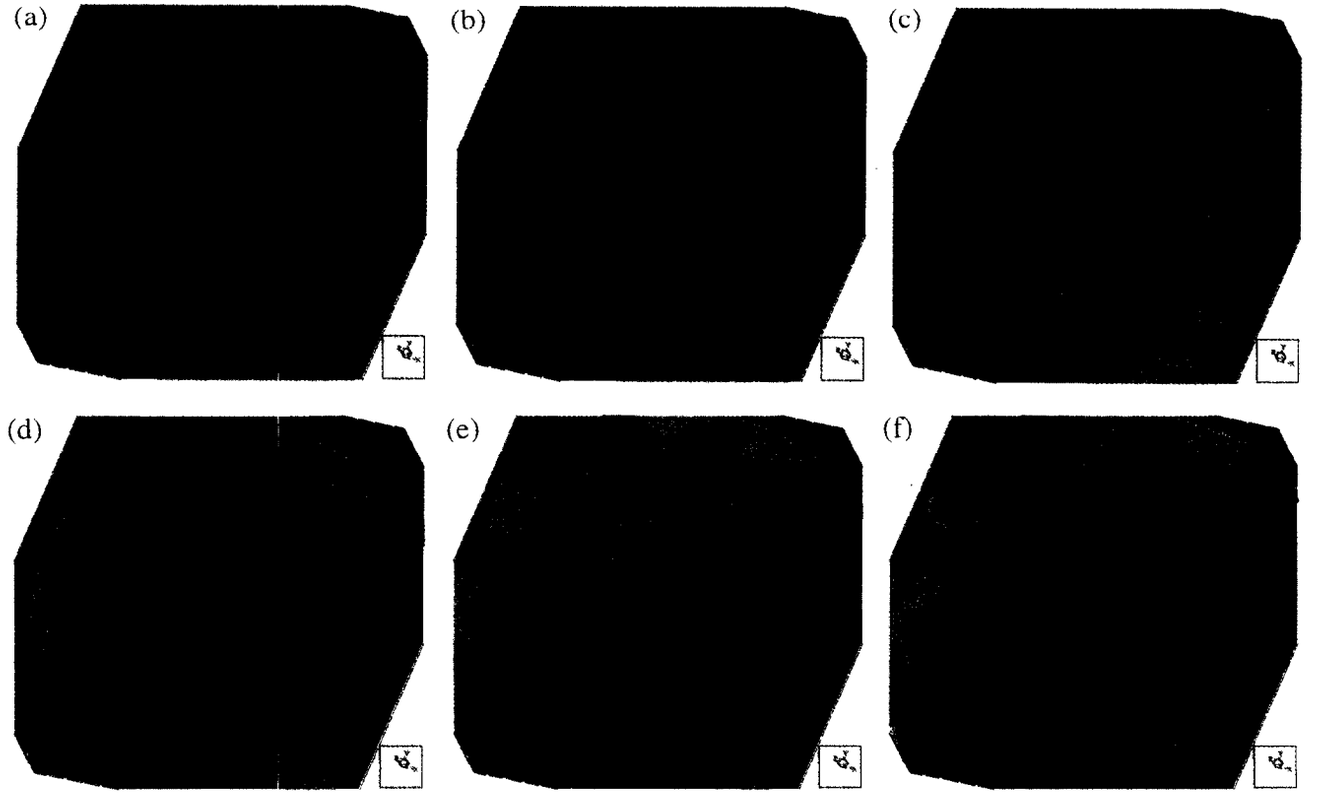

Fig. 18. Computed 3D isosurfaces of 50% temperature for the 3D thermohaline Elder problem (viewing from top to bottom) at $B = 5$ and times of (a) 1; (b) 2; (c) 4; (d) 10; (e) 15 and (f) 20 years.

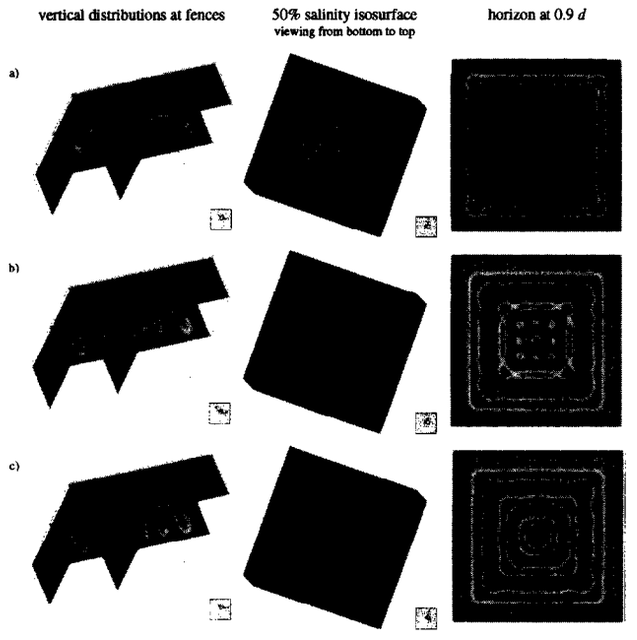

Fig. 19. Computed salinity patterns for the 3D Bénard convection problem at Rayleigh number of 200 and dimensionless times of (a) 0·013; (b) 0·026 and (c) 0·078.

The interaction between solutal and thermal convection is studied by varying the buoyancy ratio B, which expresses the relationship between buoyancy forces due to solutal and thermal convection. Differences between (pure) saline convection and thermohaline convection become apparent for buoyancy ratios $B \leq 5$. We found asymmetric convection patterns for buoyancy ratios near to unity. In this situation, the hydrodynamic system becomes strongly unstable because the solutal and thermal buoyancy effects are nearly equilibrated. As a result, very small vertical velocities trigger the convection process. Grid effects indicate the physical instability. The numerical solution of thermohaline convection systems with buoyancy ratios near to unity requires extremely fine spatial discretizations.

Three-dimensional convection needs sufficiently high spatial and temporal resolutions if damping measures, such as upwinding, are to be avoided. At moderate Rayleigh numbers (400 for the 3D Elder problem and 200 for the 3D Bénard convection) we used more than 50 000 nodes for a quarter of the domain and about 230 000 nodes for the total discretization of a 3D porous layer subjected to a free convection process. In comparison with 2D, where it has been found that about 10 000 nodes are required to accomplish satisfactorily accurate results for the Elder problem, the chosen 3D resolution seems to be a minimum for this class of problems. Time marching is based on a predictor-corrector strategy with an automatic time step control embedded in a one-step full Newton method. For the present examples more than 600 intrinsic time steps are required for simulating a 3D convection process with a duration of about 20 years for a convergence tolerance γ of 10^{-3}.

It becomes clear that a long-term analysis of 3D free or thermohaline convection takes a large numerical effort and is normally a time-consuming task. While a 2D simulation is still on the order of hours of CPU time, a 3D problem can take days of runtime on a workstation. However, by using a high-speed workstation available today the 3D Elder problems and the Bénard convection could be solved in one day and two days of runtime, respectively. It should be taken into consideration that the FEFLOW code is general and not streamlined, for instance, for special cases of free convection in rectangular domains with homogeneous parameters. That means the impact and the found efforts are representative for general problems having an arbitrary geometry and permitting such parametric and boundary conditions which are required in actual site-specific applications.[19]

REFERENCES

1. Ackerer, P., Mosé, R., Siegel, P. & Chavent, G., Reply to contribution of reference 11. *Water Resour. Res.*, **32** (1996) 1911–1913.
2. Angisara, D. & Scrinivasan, J., Natural convection flows due to the combined buoyancy of heat and mass diffusion in a thermally stratified medium. *J. Heat Transfer*, **111** (1989) 657–663.
3. Axelsson, O., *Iterative Solution Methods*, Cambridge University Press, 1994.
4. Beauwens, R., Modified incomplete factorization strategies. In: *Preconditioned Conjugate Gradient Methods, Lecture Notes in Mathematics*, 1457, ed. O. Axelsson & L. Kolotilina, Springer, New York, 1990, 1–16.
5. Behie, A. & Vinsome, P. K. W., Block iterative methods for fully implicit reservoir simulation. *SPEJ Soc. Pet. Eng. J.*, (October 1981) 658–668.
6. Beukema, K. J. & Bruin, S., Three-dimensional natural convection in a confined porous medium with internal heat generation. *Int. J. Heat Mass Transfer*, **26** (1983) 451–458.
7. Bixler, N. E., An improved time integrator for finite element analysis. *Communications in Applied Numerical Methods*, **5** (1989) 69–78.
8. Brandt, A. & Fernando, H. J. S. (Eds), *Double-diffusive Convection*, Geophysical Monograph Vol. 94, American Geophysical Union, Washington, D.C., 1995.
9. Caltagirone, J. P., Meyer, G. & Mojtabi, A., Structurations thermoconvectives tridimensionelles dans une couche poreuse horizontale. *J. Mécanique*, **20** (1981) 219–232.
10. Chan, Y. T. & Banerjee, S., Analysis of transient three-dimensional natural convection in porous media. *ASME J. Heat Transfer*, **103** (1981) 242–248.
11. Cordes, Ch. & Kinzelbach, W., Comment on contribution of reference 51. *Water Resour. Res.*, **32** (1996) 1905–1909.
12. Croucher, A. E. & O'Sullivan, M. J., The Henry problem for saltwater intrusion. *Water Resour. Res.*, **31** (1995) 1809–1814.
13. Diersch, H.-J., Primitive variables finite element solutions of free convection flows in porous media. *Zeitschr. Angew. Math. Mech. (ZAMM)*, **61** (1981) 325–337.
14. Diersch, H.-J., Study of free convective flows in porous media and effects of mechanical dispersion using finite element methods. *Gerlands Beiträge zur Geophysik*, **90** (1981) 489–506.

15. Diersch, H.-J., On finite element upwinding and its numerical performance in simulating coupled convective transport processes. *Zeitschr. Angew. Math. Mech. (ZAMM)*, **63** (1983) 479–488.
16. Diersch, H.-J., Prochnow, D. & Thiele, M., Finite element analysis of dispersion-affected saltwater upconing below a pumping well. *Appl. Math. Modelling*, **8** (1984) 305–312.
17. Diersch, H.-J., Finite element modelling of recirculating density-driven saltwater intrusion processes in groundwater. *Adv. Water Resour.*, **11** (1988) 25–43.
18. Diersch, H.-J. G., Computational aspects in developing an interactive 3D groundwater transport simulator using FEM and GIS. *Groundwater Quality Management* (Proceedings of the GQM 93 Conference held at Tallinn, September 1993). IAHS Publ. no. 220, 1994, 313–326.
19. Diersch, H.-J., Albert, H., Schreyer, J. & Richter, J., Three-dimensional modeling of flow and contaminant transport processes arising in flooding the Königstein uranium pit. In: *Proc. Intern. Conf. Uranium-Mining and Hydrogeology*, eds. B. Merkel *et al.* Verlag Sven von Loga, Köln, 1995, 121–130.
20. Diersch, H.-J. G., Interactive, graphics-based finite-element simulation system FEFLOW for modeling groundwater flow, contaminant mass and heat transport processes, *User's Manual Version 4.5*, April 1996, WASY Institute for Water Resources Planning and Systems Research Ltd, Berlin.
21. Diersch, H.-J. G. & Kolditz, O., On finite-element analysis of spatio-temporal buoyancy-driven convection processes in porous media. *Calibration and Reliability in Groundwater Modelling* (Proceedings of the ModelCARE 96 Conference held at Golden, Colorado, September 1996), IAHS Publ. no. 237, 1996, 407–415.
22. Diersch, H.-J. G., FEFLOW — Physical basis of modeling, WASY Ltd., Berlin, November 1996, 82p.
23. Elder, J. W., Transient convection in a porous medium. *J. Fluid Mech.*, **27**, Part 3 (1967) 609–623.
24. Evans, G. E. & Nunn, J. A., Free thermohaline convection in sediments surrounding a salt column. *J. Geophys. Res.*, **94** (1989) 12413–12422.
25. Fan, Y. & Kahawita, R., A numerical study of variable density flow and mixing in porous media. *Water Resour. Res.*, **30** (1994) 2707–2716.
26. Frind, E. O., Simulation of long-term transient density-dependent transport in groundwater. *Adv. Water Resour.*, **5** (1982) 73–88.
27. Galeati, G., Gambolati, G. & Neuman, S. P., Coupled and partially coupled Eulerian-Lagrangian model of freshwater-seawater mixing. *Water Resour. Res.*, **28** (1992) 149–165.
28. Gartling, D. K. & Hickox, C. E., Numerical study of the application of the Boussinesq approximation for a fluid-saturated porous medium. *Int. J. Numer. Methods Fluids*, **5** (1985) 995–1013.
29. Gresho, P. M., Lee, R. L., Chan, S. T. & Leone Jr., J. M., A new finite element for Boussinesq fluids. *Pre-print UCRL-82842*, Lawrence Livermore Laboratory, University of California, 1979, 12p.
30. Gresho, P. M., Lee, R. L. & Sani, R. L., On the time-dependent solution of the incompressible Navier-Stokes equations in two and three dimensions. *Preprint UCRL-83282*, Lawrence Livermore Laboratory, University of California, 1979, 53p.
31. Hassanizadeh, M. S. & Leijnse, A., On the modeling of brine transport in porous media. *Water Resour. Res.*, **24** (1988) 321–330.
32. Herbert, A. W., Jackson, C. P. & Lever, D. A., Coupled groundwater flow and solute transport with fluid density strongly dependent upon concentration. *Water Resour. Res.*, **24** (1988) 1781–1795.
33. Hestenes, M. R. & Stiefel, E., Methods of conjugate gradients for solving linear systems. *J. Res. Natl. Bur. Stand. Sect. B*, **49** (1952) 409–436.
34. Holst, P. H. & Aziz, K., Transient three-dimensional natural convection in confined porous media. *Int. J. Heat Mass Transfer.*, **15** (1972) 73–90.
35. Horne, R. N. & O'Sullivan, M. J., Oscillatory convection in a porous medium heated from below. *J. Fluid Mech.*, **66** (1974) 339–352.
36. Horne, R. N., Three-dimensional natural convection in a confined porous medium heated from below. *J. Fluid Mech.*, **92** (1979) Part 4, 751–766.
37. Horne, R. N. & Caltagirone, J. P., On the evaluation of thermal disturbances during natural convection in a porous medium. *J. Fluid Mech.*, **100** (1980) 385–395.
38. Huyakorn, P. S. & Taylor, C., Finite element models for coupled groundwater and convective dispersion. *Proc. 1st Int. Conf. Finite Elements in Water Resources*, ed. Gray, W. G. *et al.* Princeton University, July 1976, Pentech Press, London, 1977, 1.131–1.151.
39. Huyakorn, P. S., Anderson, P. F., Mercer, J. W. & White, Jr., H. O., Saltwater intrusion in aquifers: development and testing of a three-dimensional finite element model. *Water Resour. Res.*, **23** (1987) 293–312.
40. Kakinuma, T., Kishi, Y. & Inouchi, K., The behaviour of groundwater with dispersion in coastal aquifers. *J. Hydrology*, **98** (1988) 225–248.
41. Knaber, P. & Frolkovic, P., Consistent velocity approximation for finite volume or element discretization of density driven flow in porous media. *Proc. XI. Int. Conf. Computational Methods in Water Resources* held in Cancun, México, July 1996, *Comp. Mech. Publ.*, Vol. 1, ed. Aldama *et al.* Southampton, 1996, 93–100.
42. Kolditz, O., Benchmarks for numerical groundwater simulations, In: FEFLOW User's Manual, Chapter 5, H.-J. G. Diersch, WASY Ltd, Berlin, 1996.
43. Kolditz, O., Ratke, R., Diersch, H.-J. G. & Zielke, W., Coupled groundwater flow and transport: 1, Verification of variable-density flow and transport models. *Adv. Water Resour.*, **21** (1998) 27–46.
44. Konikow, L. F., Campbell, P. J. & Sanford, W. E., Modelling brine transport in a porous medium: a re-evaluation of the HYDROCOIN Level 1, Case 5 problem. *Calibration and Reliability in Groundwater Modelling* (Proceedings of the ModelCARE 96 Conference held at Golden, Colorado, September 1996), IAHS Publ. no. 237, 1996, 363–372.
45. Lee, R. L., Gresho, P. M. & Sani, R. L., Numerical smoothing techniques applied to some finite element solutions of the Navier-Stokes equations. *Proc. 1st Int. Conf. Finite Elements in Water Resources*, ed. Gray, W. G. *et al.* Princeton University, July 1976, Pentech Press, London, 1977, 4.127–4.145.
46. Leijnse, A., Three-dimensional modeling of coupled flow and transport in porous media. Dissertation, University of Notre Dame, Indiana (USA), 1992.
47. Letniowski, F. W., An overview of preconditioned iterative methods for sparse matrix equations. Research Report CS-89-26, Faculty of Mathematics, University of Waterloo, Canada, 1989, 32p.
48. Lever, D. A. & Jackson, C. P., On the equations for the flow of concentrated salt solution through a porous medium. U.K. DOE Report No. DOE/RW/85.100, 1985.
49. Meijerink, J. A. & Van der Vorst, H. A., Guidelines for the usage of incomplete decomposition in solving sets of linear systems as they occur in practical problems. *J. Comput. Physics.*, **44** (1981) 134–155.

50. Mercer, J. W. & Pinder, G. F., Finite element analysis of hydrothermal systems. *Finite Element Methods in Flow Problems* (Proc. 1st Symp., Swansea, 1974), ed. Oden, J. T. *et al.* University of Alabama Press, 1974, 401–414.
51. Mosé, R., Siegel, P., Ackerer, P. & Chavent, G., Application of the mixed hybrid finite element approximation in a groundwater flow model: Luxury or necessity? *Water Resour. Res.*, **30** (1994) 3001–3012.
52. Murray, B. T. & Chen, C. F., Double-diffusive convection on a porous medium. *J. Fluid Mech.*, **201** (1989) 147–166.
53. Nield, D. A., Onset of thermohaline convection in a porous medium. *Water Resour. Res.*, **11** (1968) 553–560.
54. Nield, D. A. & Bejan, A., *Convection in Porous Media*, Springer Verlag, Berlin, 1992.
55. Oldenburg, C. M. & Pruess, K., Dispersive transport dynamics in a strongly coupled groundwater-brine system. *Water Resour. Res.*, **31** (1995) 289–302.
56. Perrochet, P., Personal communication. EPFL Lausanne, GEOLEP Laboratoire de géologie, Lausanne (Switzerland), 1996.
57. Pinder, G. F. & Cooper, H. H., A numerical technique for calculating the transient position of the saltwater front. *Water Resour. Res.*, **6** (1970) 875–882.
58. Riley, D. S. & Winters, K. H., Time-periodic convection in porous media: the evolution of Hopf bifurcations with aspect ratio. *J. Fluid Mech.*, **223** (1991) 457–474.
59. Rubin, H., Onset of thermohaline convection in a cavernous aquifer. *Water Resour. Res.*, **12** (1976) 141–147.
60. Rubin, H. & Roth, C., Thermohaline convection in flowing groundwater. *Adv. Water Resour.*, **6** (1983) 146–156.
61. Saad, Y. & Schultz, M. H., GMRES: A generalized minimal residual algorithm for solving nonsymmetric linear systems. *SIAM J. Sci. Stat. Comp.*, **7** (1986) 856–869.
62. Sauter, F. J. & Beusen, A. H. W., Streamline calculations using continuous and discontinuous velocity fields and several time integration methods. *Groundwater Quality Management* (Proc. of the GQM 93 Conf. held at Tallinn, Sept. 1993). IAHS Publ. no. 220, 1994, 347–355.
63. Schincariol, R. A., Schwartz, F. W. & Mendoza, C. A., On the generation of instabilities in variable density flow. *Water Resour. Res.*, **30** (1994) 913–927.
64. Schubert, G. & Straus, J. M., Three-dimensional and multicellular steady and unsteady convection in fluid-saturated porous media at high Rayleigh numbers. *J. Fluid Mech.*, **94** (1979) Part 1, 25–38.
65. Schubert, G. & Straus, J. M., Transitions in time-dependent thermal convection in fluid-saturated porous media. *J. Fluid Mech.*, **121** (1982) 301–303.
66. Segol, G., Pinder, G. F. & Gray, W. G., A Galerkin finite element technique for calculating the transient position of the saltwater front. *Water Resour. Res.*, **11** (1975) 343–347.
67. Shen, C. Y., The evolution of the double-diffusive instabilities: salt fingers. *Phys. Fluids*, **A1** (1989) 5.
68. Sonneveld, P., CGS, a fast Lanczos-type solver for nonsymmetric linear systems. *SIAM J. Sci. Stat. Comp.*, **10** (1989) 36–52.
69. Straus, J. M. & Schubert, G., Three-dimensional convection in a cubic box of fluid-saturated porous material. *J. Fluid Mech.*, **91** (1979) Part 1, 155–165.
70. Straus, J. M. & Schubert, G., Modes of finite-amplitude three-dimensional convection in rectangular boxes of fluid-saturated material;. *J. Fluid Mech.*, **103** (1981) 23–32.
71. Tong, C. H., A comparative study of preconditioned Lanczos methods for nonsymmetric linear systems. *Sandia Report SAND91-8240*, Sandia National Lab., Albuquerque, Sept. 1992, 118p.
72. Trevisan, O. V. and Bejan, A., Natural convection with combined heat and mass transfer buoyancy effects in a porous medium. *Int. J. Heat Mass Transfer*, **28** (1985) 1597–1611.
73. Tyvand, P. A., Thermohaline instability in anisotropic porous media. *Water Resour. Res.*, **16** (1980) 325–330.
74. Van der Vorst, H. A., Bi-CGSTAB: A fast and smoothly convergent variant of BiCG for the solution of nonsymmetric linear systems. *SIAM J. Sci. Stat. Comp.*, **13** (1992) 631–644.
75. Voss, C. I. & Souza, W. R., Variable density flow and solute transport simulation of regional aquifers containing a narrow freshwater-saltwater transition zone. *Water Resour. Res.*, **26** (1987) 2097–2106.
76. Xue, Y., Xie, C., Wu, J., Liu, P., Wang, J. & Jiang, Q. A three-dimensional miscible transport model for seawater intrusion in China. *Water Resour. Res.*, **31** (1995) 903–912.
77. Yeh, G. T., On the computation of Darcian velocity and mass balance in the finite element modeling of groundwater flow. *Water Resour. Res.*, **17** (1981) 1529–1534.
78. Zebib, A. & Kassoy, D. R., Three-dimensional natural convection motion in a confined medium. *Phys. Fluids*, **21** (1978) 1–3.
79. Zhang, H. & Schwartz, F. W., Multispecies contaminant plumes in variable density flow systems. *Water Resour. Res.*, **31** (1995) 837–847.

APPENDIX A

Weak form of the continuity eqn (1)

The weak form of the continuity eqn (1) gives

$$\int_\Omega w S_o \frac{\partial h}{\partial t} - \int_\Omega \frac{\partial w}{\partial x_i} q_i^{\mathrm{f}} = -\int_\Gamma w q_i^{\mathrm{f}} n_i + \int_\Omega w(Q_\rho + Q_{\mathrm{EB}}) \tag{A1}$$

Introducing the Darcy eqn (2) into eqn (1) and taking into account that the buoyancy term leads to

$$\frac{\rho^{\mathrm{f}} - \rho_o^{\mathrm{f}}}{\rho_o^{\mathrm{f}}} = \frac{\bar{\alpha}}{(C_{\mathrm{s}} - C_o)}(C - C_o) - \bar{\beta}(T - T_{\mathrm{o}}) \tag{A2}$$

by using the fluid density equation of state (5), following final weighted residual formulation of the continuity equation results

$$\begin{aligned}
&\int_\Omega w S_o \frac{\partial h}{\partial t} + \int_\Omega \frac{\partial w}{\partial x_i} K_{ij} f_\mu \frac{\partial h}{\partial x_j} \\
&\quad = -\int_\Omega \frac{\partial w}{\partial x_i} K_{ij} f_\mu \left[\frac{\bar{\alpha}}{(C_{\mathrm{s}} - C_o)}(C - C_o) \right. \\
&\qquad \left. - \bar{\beta}(T - T_o) \right] e_j \\
&\qquad - \int_\Omega w q_i^{\mathrm{f}} \left(\frac{\bar{\alpha}}{(C_{\mathrm{s}} - C_o)} \frac{\partial C}{\partial x_i} - \bar{\beta} \frac{\partial T}{\partial x_i} \right) \\
&\qquad - \int_\Omega w \epsilon \left(\frac{\bar{\alpha}}{(C_{\mathrm{s}} - C_o)} \frac{\partial C}{\partial t} - \bar{\beta} \frac{\partial T}{\partial t} \right) \\
&\qquad - \int_\Gamma w \underbrace{q_i^{\mathrm{f}} n_i}_{q_{n_{\mathrm{h}}}} + \int_\Omega w Q_\rho
\end{aligned} \tag{A3}$$

where the extended Boussinesq approximation term (7) is incorporated. Eqn (A3) represents the standard weak

form of the substitution formulation to solve the hydraulic head h.

Weak form of the Darcy eqn (2)

Formally, a weak form of the Darcy equation can easily be derived as

$$\int_\Omega w q_i^f = -\int_\Omega w K_{ij} f_\mu \frac{\partial h}{\partial x_j} - \int_\Omega w K_{ij} f_\mu \left[\frac{\bar{\alpha}}{(C_s - C_o)}(C - C_o) - \bar{\beta}(T - T_o) \right] e_j \tag{A4}$$

to solve the vector of Darcy fluxes q_i^f at given h, C and T.

Weak form of the mass transport eqns (3)

The weak formulations for the divergent and convective forms of the contaminant mass conservation equations differ from the fact that for the former, the divergence theorem is applied both to the convective and the dispersive terms

$$\int_\Omega w \frac{\partial}{\partial x_i}\left(q_i^f C - D_{ij}\frac{\partial C}{\partial x_j}\right) = -\int_\Omega \frac{\partial w}{\partial x_i}\left(q_i^f C - D_{ij}\frac{\partial C}{\partial x_j}\right) + \int_\Gamma w \underbrace{\left(C q_i^f - D_{ij}\frac{\partial C}{\partial x_j}\right) n_i}_{q_{n_c}^{\text{total}}} \tag{A5}$$

while the conventional convective form applies the divergence theorem only to the dispersive (second order) term

$$\int_\Omega w \frac{\partial}{\partial x_i}\left(D_{ij}\frac{\partial C}{\partial x_j}\right) = -\int_\Omega \frac{\partial w}{\partial x_i} D_{ij}\frac{\partial C}{\partial x_j} + \int_\Gamma w \underbrace{D_{ij}\frac{\partial C}{\partial x_j} n_i}_{-q_{n_c}^{\text{disp}}} \tag{A6}$$

Finally, it yields the following weak formulations

$$\int_\Omega w R_d \frac{\partial C}{\partial t} - \int_\Omega \frac{\partial w}{\partial x_i} q_i^f C + \int_\Omega \frac{\partial w}{\partial x_i} D_{ij}\frac{\partial C}{\partial x_j} + \int_\Omega w R\theta C = \int_\Omega w Q_C - \int_\Gamma w q_{n_c}^{\text{total}} \tag{A7}$$

for the divergent form and

$$\int_\Omega w R_d \frac{\partial C}{\partial t} + \int_\Omega w q_i^f \frac{\partial C}{\partial x_i} + \int_\Omega \frac{\partial w}{\partial x_i} D_{ij}\frac{\partial C}{\partial x_j} + \int_\Omega w(R\theta + Q_p) C = \int_\Omega w Q_C - \int_\Gamma w q_{n_c}^{\text{disp}} \tag{A8}$$

for the convective form, respectively, to solve the concentration C.

Weak form of the heat transport eqn (4)

Similar to the above, the weak formulation of the convective form of the heat transport equation is given by

$$\int_\Omega w\left[\epsilon\rho^f c^f + (1-\epsilon)\rho^s c^s\right]\frac{\partial T}{\partial t} + \int_\Omega w \rho^f c^f q_i^f \frac{\partial T}{\partial x_i} + \int_\Omega \frac{\partial w}{\partial x_i}\lambda_{ij}\frac{\partial T}{\partial x_j} = \int_\Omega w Q_T - \int_\Gamma w q_{n_T}^{\text{cond}} \tag{A9}$$

for solving the temperature T.

Finite element formulations

Employing the Galerkin version of the FEM (GFEM), $w_m = N_m$, for the above weak formulations and replacing the h, q_i^f, C and T variables by their trial approximations

$$\left.\begin{aligned} h(x_i,t) &\cong \hat{h}(x_i,t) = \sum_m N_m(x_i) h_m(t) \\ q_i^f(x_i,t) &\cong \hat{q}_i^f(x_i,t) = \sum_m N_m(x_i) q_{im}^f(t) \\ C(x_i,t) &\cong \hat{C}(x_i,t) = \sum_m N_m(x_i) C_m(t) \\ T(x_i,t) &\cong \hat{T}(x_i,t) = \sum_m N_m(x_i) T_m(t) \end{aligned}\right\} \tag{A10}$$

the matrix coefficients of eqn (8) are as follows

$$\left.\begin{aligned} O_{mn} &= \int_\Omega S_o N_m N_n \qquad A_{mn} = \int_\Omega N_m N_n \\ P_{mn} &= \int_\Omega R_d N_m N_n \\ U_{mn} &= \int_\Omega \left[\epsilon\rho^f c^f + (1-\epsilon)\rho^s c^s\right] N_m N_n \end{aligned}\right\} \tag{A11}$$

$$S_{mn} = \int_\Omega K_{ij} f_\mu \frac{\partial N_m}{\partial x_i}\frac{\partial N_n}{\partial x_j} \tag{A12}$$

$$\left.\begin{aligned} D_{mn} &= \int_\Omega \left[-\frac{\partial N_m}{\partial x_i}\hat{q}_i^f N_n + D_{ij}\frac{\partial N_m}{\partial x_i}\frac{\partial N_n}{\partial x_j} + R\theta N_m N_n \right] \quad \text{divergent form} \\ D_{mn} &= \int_\Omega \left[N_m \hat{q}_i^f \frac{\partial N_n}{\partial x_i} + D_{ij}\frac{\partial N_m}{\partial x_i}\frac{\partial N_n}{\partial x_j} + (R\theta + Q_\rho) N_m N_n \right] \quad \text{convective form} \end{aligned}\right\} \tag{A13}$$

$$L_{mn} = \int_\Omega \left[N_m \rho^f c^f \hat{q}_i^f \frac{\partial N_n}{\partial x_i} + \lambda_{ij}\frac{\partial N_m}{\partial x_i}\frac{\partial N_n}{\partial x_j}\right] \tag{A14}$$

$$F_m = -\int_\Omega \frac{\partial N_m}{\partial x_i} K_{ij} f_\mu \left[\frac{\bar{\alpha}}{(C_s - C_o)} (\hat{C} - C_o) - \bar{\beta}(\hat{T} - T_o) \right] e_j - \int_\Omega N_m \hat{q}_i^f \left(\frac{\bar{\alpha}}{(C_s - C_o)} \frac{\partial \hat{C}}{\partial x_i} - \bar{\beta} \frac{\partial \hat{T}}{\partial x_i} \right) - \int_\Omega N_m \epsilon \left(\frac{\bar{\alpha}}{(C_s - C_o)} \frac{\partial \hat{C}}{\partial t} - \bar{\beta} \frac{\partial \hat{T}}{\partial t} \right) - \int_\Gamma N_m q_{n_h} + \int_\Omega N_m Q_\rho \quad \text{(A15)}$$

$$B_{im} = -\int_\Omega N_m K_{ij} f_\mu \frac{\partial \hat{h}}{\partial x_j} - \int_\Omega N_m K_{ij} f_\mu \left[\frac{\bar{\alpha}}{(C_s - C_o)} (\hat{C} - C_o) - \bar{\beta}(\hat{T} - T_o) \right] e_j \quad \text{(A16)}$$

$$\left.\begin{aligned} R_m &= \int_\Omega N_m Q_C - \int_\Gamma N_m q_{n_c}^{\text{total}} \quad \text{divergent form} \\ R_m &= \int_\Omega N_m Q_C - \int_\Gamma N_m q_{n_c}^{\text{disp}} \quad \text{convective form} \end{aligned}\right\} \quad \text{(A17)}$$

$$W_m = \int_\Omega N_m Q_T - \int_\Gamma N_m q_{n_T}^{\text{cond}} \quad \text{(A18)}$$

APPENDIX B

Global smoothing of discontinuous velocity fields

A global approximation of the smoothed Darcy velocities can be written as

$$q_i^f(x_i) = \sum_m N_m(x_i) q_{im}^f \quad \text{(B1)}$$

Assume that we have an unsmoothed (discontinuous) velocity field $q_i^{f*}(x_i)$, then the smooth function which provides a best fit in the least squares sense over the domain Ω can be obtained from a minimization of the functional

$$J = \int_\Omega \left(q_i^f - q_i^{f*} \right)^2 \Rightarrow \text{Min} \quad \text{(B2)}$$

The minimilization procedure

$$\frac{\partial J}{\partial q_{im}^f} = \int_\Omega 2\left(q_i^f - q_i^{f*} \right) \frac{\partial q_i^f}{\partial q_{im}^f} = 0 \quad \text{for} \quad m = 1, 2, \ldots \quad \text{(B3)}$$

or

$$\int_\Omega N_m \left(q_i^f - q_i^{f*} \right) = 0 \quad \text{(B4)}$$

results in a system of linear equations to solve the smoothed velocities q_i^f, namely

$$\sum_n M_{mn} q_{in}^f = Z_{im} \quad \text{(B5)}$$

where M_{mn} represents the mass matrix and Z_{im} is the RHS involving the unsmoothed relations. They are formed in the finite element assembling procedure as

$$M_{mn} = \int_\Omega N_m N_n \quad \text{(B6)}$$

and, by inserting the Darcy velocity components, as

$$Z_{im} = \int_\Omega N_m q_i^{f*} = -\int_\Omega N_m \left[K_{ij} f_\mu \left(\frac{\partial \hat{h}}{\partial x_j} + \left[\frac{\bar{\alpha}}{(C_s - C_o)} (\hat{C} - C_o) - \bar{\beta}(\hat{T} - T_o) \right] e_j \right) \right] \quad \text{(B7)}$$

Note, the least square approximations of global smoothing (B7) is equivalent to the Galerkin weighting procedure (A16) in Appendix A.

A cost-effective alternative appears if the mass matrix M_{mn} is lumped by an row-sum or diagonal scaling

$$M_{mn} = \begin{cases} \int_\Omega N_m \left(\sum N_n \right) & m = n \\ 0 & m \neq n \end{cases} \quad \text{(B8)}$$

without need to solve the linear equation system (B5). Mass lumping can be shown to be equivalent to an area-weighted averaging for nodal values.

Local smoothing of discontinuous velocity fields

Unlike global smoothing, there is an efficient way to smooth velocity fields by using only individual element information. This is termed as local smoothing[45] and provides a simple nodal averaging based on the number of elements joined at a given mode (element patch). Among several approaches suggested FEFLOW employs the following two-step local technique.

Step 1. The discontinuous velocity in each element e

$$q_{ip}^{f*e} = -K_{ij} f_\mu \left(\frac{\partial \hat{h}^e}{\partial x_j} + \left[\frac{\bar{\alpha}}{(C_s - C_o)} (\hat{C}^e - C_o) - \bar{\beta}(\hat{T}^e - T_o) \right] e_j \right) \quad \text{(B9)}$$

is computed at the Gauss points p ($2 \times 2(\times 2)$ for linear and $3 \times 3(\times 3)$ for quadratic elements) with given approximations of the hydraulic head $\hat{h}^e$, concentration $\hat{C}^e$, and temperature $\hat{T}^e$ for element e from previous solutions.

Step 2. The values at the Gauss points are assigned to

the nearest corner node $p \rightarrow m$. Each nodal contribution is summed up and, at the end, the nodal values are averaged by their number of nodal contributions n_p from the patch sharing the node m

$$q^f_{im} = \left(\sum_e^{\text{patch}} q^{f*e}_{im} \right) / n_p \tag{B10}$$

APPENDIX C

Auxiliary problem formulation used for budget flux computation of the convective part

The budget analysis aims at the computation of the normal convective mass (or heat) fluxes $Q^R_C = \sum \int_\Gamma (C^R q^R_{n_h})$. Multiplying each term of the continuity eqn (1) by concentration C we get the weak form

$$\int_\Omega wC \frac{\partial q^f_i}{\partial x_i} = \int_\Omega wC(Q_\rho + Q_{EB}) - \int_\Omega wCS_o \frac{\partial h}{\partial t} \tag{C1}$$

It is further

$$\frac{\partial (wCq^f_i)}{\partial x_i} = Cq^f_i \frac{\partial w}{\partial x_i} + wC \frac{\partial q^f_i}{\partial x_i} + wq^f_i \frac{\partial C}{\partial x_i} \tag{C2}$$

Employing the divergence theorem on the LHS of identity (C2) we obtain from (C1) and (C2)

$$\int_\Gamma wCq^f_i n_i = \int_\Omega C \frac{\partial w}{\partial x_i} q^f_i + \int_\Omega w \frac{\partial C}{\partial x_i} q^f_i + \int_\Omega wC(Q_\rho + Q_{EB}) - \int_\omega wCS_o \frac{\partial h}{\partial t} \tag{C3}$$

It has been found to evaluate the individual terms of eqn (C3) in different ways. While the velocity q^f_i in the first term of the RHS is expressed by the Darcy law, the second RHS term uses explicitly the velocity from the computation. The LHS surface integral describes already the desired convective mass flux along the boundary portion Γ, where $q^R_{n_h} = q^f_i n_i|_R$ is the normal fluid flux and $q^R_{n_C} = Cq^f_i n_i|_R = Cq_{n_h}|_R$ is the normal convective mass flux through the boundary.

Finally, following finite element formulation results in computing the normal convective mass flux from given solutions (A10) of hydraulic head $\hat{h}$, Darcy flux $\hat{q}^f_i$, concentration $\hat{C}$, and temperature $\hat{T}$

$$\begin{aligned} \int_\Gamma N_m q^R_{n_c} = &- \int_\Omega K_{ij} f_\mu \frac{\partial N_m}{\partial x_i} \frac{\partial N_n}{\partial x_j} (N_k C_k) h_n \\ &- \int_\Omega K_{ij} f_\mu \frac{\partial N_m}{\partial x_i} (N_k C_k) \left[\frac{\bar{\alpha}}{(C_s - C_o)} (\hat{C} - C_o) - \bar{\beta}(\hat{T} - T_o) \right] e_j \\ &+ \int_\Omega N_m \left(\frac{\partial N_n}{\partial x_i} C_n \right) \left(N_k q^f_{ik} \right) \\ &+ \int_\Omega N_m (N_n C_n)(Q_\rho + Q_{EB}) \\ &- \int_\Omega N_m (N_n C_n) S_o \left(N_k \frac{\partial h_k}{\partial t} \right) \end{aligned} \tag{C4}$$

All contributions of mass flux are summed up at node m to obtain the lumped nodal balance mass flux Q^R_C in the form

$$Q^R_C = - \int_\Gamma q^R_C = - \sum_e \int_{\Gamma^e} N_m q^R_{n_c} \tag{C5}$$

which is defined positive inward and will be used for the boundary constraint control (see Section 6). Similar expressions to (C4) and (C5) can be derived for heat balance fluxes if $\rho^f c^f T$ is used as a multiplier.